



PHAS0097: Astrophysics/Physics Project:

**Watching Wiggling Biomolecules with Atomic Force
Microscopy**



Joshua Giblin-Burnham
Supervisor: Prof. Bart Hoogenboom

Theoretical Physics (MSci)
Faculty of Mathematical and Physical Sciences
Department of Physics and Astronomy

Word Count: 7480

University College London

April 2023

Abstract

Atomic Force Microscopy (AFM) is a versatile three-dimensional topographic technique implementing a mechanical probe to raster-scan and image sample surfaces. The technique provides reliable nanometer measurements of materials^{1–4} and has become a valuable tool with a diverse range of applications in areas such as materials physics, nanotechnology, electronics, and biology^{3,5,6}. However, there are limited computational recreations of AFM imaging, and the area could benefit from greater tools to aid in interpreting surface characteristics. Consequently, this research presents novel computational modelling of AFM imaging, specifically for biomolecular samples. Currently, simulations of AFM imaging use a hard-sphere model and neglect tip indentation⁷. This research implemented Finite Element Modelling (FEM) and the commercial software ABAQUS to simulate AFM tip indentation and produce force curves that accounted for contact dynamics. Initial tests verified the accuracy of ABAQUS, focusing on the indentation of elastic half-spaces and spheres. The elastic half-space simulations showed good agreement with the theoretical models. In contrast, the results indicate that simple Hertzian models underestimate the elastic modulus of spherical samples and instead require Double Contact models. Moreover, a novel formulation of the Double Contact model for conical indenters demonstrated significant predictive power over a range of surface radii. Next, a FEM approach was applied to analyse the compression of simple hemispheres and periodic surfaces during AFM imaging. These simulations highlighted the dependency of the elastic behaviour on the contact radius and tip convolution. Our results indicated that larger indenters require larger forces to compress the sample to the same extent. In addition, Fourier analysis of the simulated AFM contours elucidated a possible novel trend, that larger indentation forces recover more of a surface's periodicity. Finally, a FEM simulation of AFM imaging was applied to simulate the appearance of B-DNA Dodecamer. Simulations used an assembly of the AFM tip and the biomolecule surface to produce individual indentations across the sample. Subsequently, contours of constant force are used to return an AFM image. These simulations show the viability of the FEM approach in reproducing the AFM dynamics and provide a wealth of extensions to be explored.

Contents

Abstract	1
1 Introduction	3
1.1 Introduction to Atomic Force Microscopy	3
1.2 Previous Simulations of Atomic Force Microscopy Images	4
1.3 A Finite Element Approach to Imaging	5
2 Methodology	6
2.1 ABAQUS Finite Element Analysis	6
2.2 Verification of Contact Models	7
2.3 Simulation of AFM Imaging	8
2.3.1 General Scan Dynamics for Imaging	8
2.3.2 Image Processing and Interpolation	9
2.3.3 Application to Biomolecules	9
2.4 Analysis of Surface Compression	11
2.4.1 Simulation Dynamics	11
2.4.2 Heat Map and Force Contours	12
2.4.3 Full Width Half Maxima	12
2.4.4 Fourier Analysis	12
2.4.5 Volume Analysis	13
2.4.6 Youngs Modulus	13
3 Results	14
3.1 FEM Verification of Contact Models	14
3.1.1 Elastic Half-space	14
3.1.2 Elastic Sphere	16
3.2 FEM Applied to Compression Simulation	19
3.2.1 Analysis of Hemisphere Structure	19
3.2.2 Analysis of a Simple Periodic Structure	21
3.3 FEM Applied to AFM Image Simulation of B-DNA	25
4 Conclusion and Discussion	27
4.1 Conclusion	27
4.2 Discussion	27
References	29
Appendix	32
A Notation	32
B Models of Indentation in Atomic Force Microscopy	33
B.1 Hertz Model	33
B.2 Other Hertzian Model	34
B.3 Dimitriadiis Model	34
B.4 Sneddon Model	34
B.5 Double Contact Model	35
B.6 Hertz Double Contact	35
B.7 Hertz-Sneddon Double Contact	36
C Tip Convolution for Hard Sphere Model	38

1 Introduction

1.1 Introduction to Atomic Force Microscopy

The Atomic Force Microscope (AFM) is a type of Scanning Probing Microscope⁸ developed by Binnig, Quate and Gerbe at IBM, Zurich^{9,10}. It uses a sharp probe tip to raster-scan a sample's topology and has become a versatile tool^{3,5,6}. The technique has various applications, for example, in atomic imaging of crystal structures¹¹ and surface measurements of materials and polymer films¹²⁻¹⁶. In addition, AFM can image under natural conditions, such as in aqueous solutions and in real-time, allowing imaging of cell dynamics and biological processes. This includes imaging protein unfolding¹⁷ and conformational changes¹⁸, alongside, characterising microbial surfaces^{19,20}. The ability to image and measure the physical properties of microbial surfaces can give important insight into microbiology, such as improving inhibition and cellular damage produced by antimicrobial compounds^{19,21}.

The imaging of AFM is based on detecting atomic forces acting between a sharp probe tip and the surface of a sample. A schematic of an AFM is shown in Figure 1. A cantilever holds the sharp tip used to probe the sample surface. A laser beam detection system using the position-sensitive photodiode (PSPD) enables the AFM system to monitor and record the deflection of the cantilever. The tip is raster-scanned across the surface of a sample, and interaction between the tip and surface causes deflection. Subsequently, the deflection is processed in the feedback system, designed to compensate for the change in topology and hold the deflective force constant during scanning. The tip deflection is compared to a reference force, producing an error signal that generates the feedback signal. The surface topography is then determined by mapping the contours of equal force²².

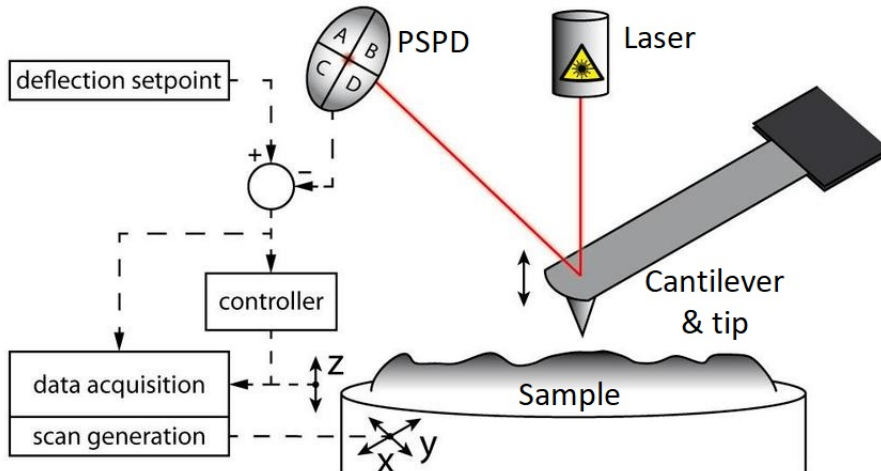


Figure 1: Schematic of AFM mechanism from Schitter *et al.*²³

However, as with any experimental technique, AFM has limitations. Various effects can lead to ambiguity in images and image artefacts. A key source of error is a consequence of the resolution being directly dependent on imaging force and the probe geometry²⁴. Imaging with large forces can dramatically reduce image resolution and damage the surface. Furthermore, probe geometry and its interaction with the sample is important to image contrast²⁴. As shown in Figure 2A, an AFM image is a convolution of the probe geometry and the sample's topology. Therefore, the tip-sample convolution produces a trace of the tip geometry over the surface, broadening protrusions and narrowing holes in the surface.

Similarly to tip convolution, AFM can produce image artefacts due to tip interaction when scanning over the edge of a surface structure. As the tip loses contact with the sample, the deflective forces diminish over the edge. As a result, the probe must increase scan depth; however, the cantilever descends at a capped rate, so the tip gradually approaches the surface,

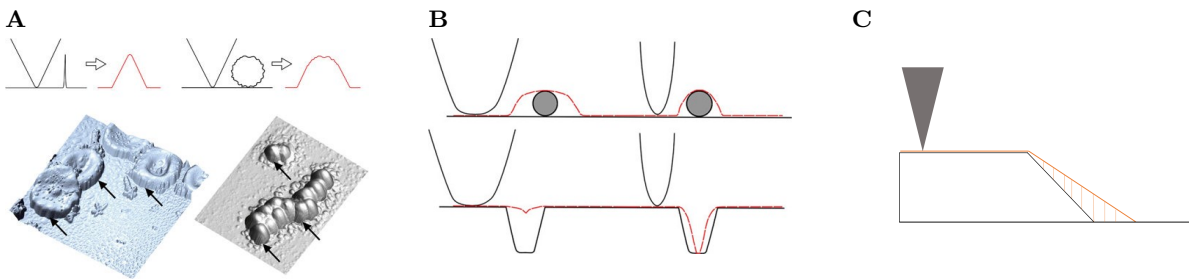


Figure 2: Illustrations of typical AFM artefacts taken or adapted from Eaton & West, Atomic Force Microscopy¹⁰. (A) Illustration of tip convolution artefact produced in AFM images. (B) Illustration of the widening/narrowing of surface features due to tip convolution. (C) Illustration of an elongated edge due to the parachuting effect.

minimising the risk of over-indenting. This causes a linearly protracted trace of the gradient and produces an elongated edge in the direction of the image scan, as shown in Figure 2C. This is known as parachuting.

Furthermore, other errors may arise due to environmental surroundings. For example, environmental vibrations can cause the probe to vibrate and produce artefacts and blur. Similarly, thermal drift is produced from prolonged usage, which causes the probe to expand/ contract thermally and produce deviations in the system. In this report, we describe computational simulations of AFM imaging to aid in interpreting images and artefacts. Moreover, we present some quantitative analysis of the compression produced in these simulations to explore the effect of imaging force and tip geometry in AFM imaging.

1.2 Previous Simulations of Atomic Force Microscopy Images

Currently, there are a limited number of AFM imaging simulations, leaving a prominent area for development. Recent work by Amyot R, Flechsig H *et al.*⁷ produced the BiomolecularAFMviewer in 2020. The BiomolecularAFMviewer, similar to this project, uses protein structural data to simulate AFM images (shown in Figure 3) and aids in interpreting experimental observations. In follow-up work in 2022, Amyot R, Flechsig H *et al.*²⁵ used the software to reconstruct resolution-limited experimental images as an example of the application of the software. The modelling used a hard sphere model of the surface and indenter, evaluating the vertical height of the tip at the initial surface-surface contact. Therefore, the simulation does not account for indentation into the surface, surface deflection, off-axial forces that produce sliding and friction, or elastic properties of the surface. This approach could be improved by accounting for force curves and the indentation of the tip with elastic properties of the material.

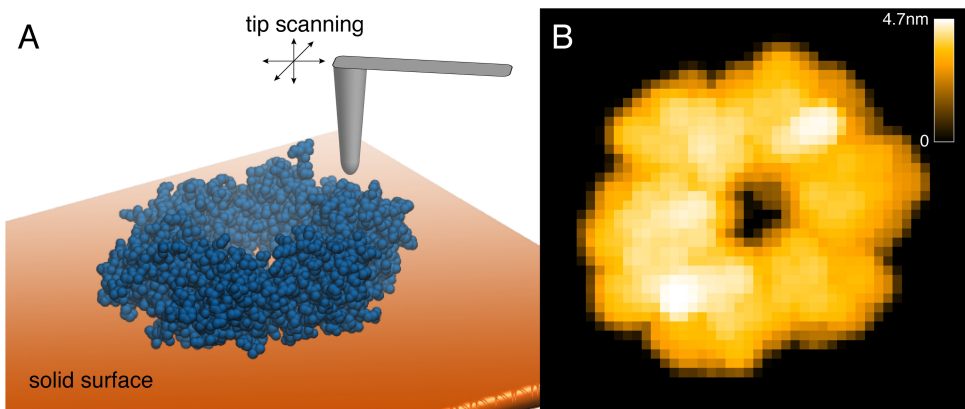


Figure 3: Graphic of simulation from BioAFMviewer⁷. (A) 3D geometry of simulation. (B) Simulated AFM image.

Other computational simulations of AFM have been used to produce such force curves that reflect these properties. However, these applications study quantitative AFM results as opposed to imaging^{26–29}. Previous work has shown the viability of the commercial software ABAQUS and Finite Element Modelling (FEM) in the study of indentation in AFM; Liu *et al.*²⁶ validated a FEM model for AFM indentation with less than 10% error when comparing the simulated force-indentation curves with the experimental data. Similar analysis of experimental data with FEM done by Roduit *et al.*³⁰ and Han *et al.*²⁷ made use of the ABAQUS software to complete calculations. The work by Rajabifar *et al.*³¹ simulated the viscoelasticity contact between an AFM tip and a surface. This showed a fast and accurate use of FEM to simulate AFM indentation and the associated force curves.

1.3 A Finite Element Approach to Imaging

Consequently, our research presents novel FEM and computational methods to model and explore AFM images, specifically in biomolecular samples. The primary work of this research focuses on improving the modelling of previous AFM simulations from a hard sphere model to a model with tip surface interactions. FEM simulations enable us to simulate tip indentation and generate force curves that incorporate more intricate forces and dynamics. We employ several FEM simulations to investigate contact models of indentation and sample compression in AFM imaging. The overall goal was to produce more accurate images and artefacts.

FEM subdivides the geometry into small, discrete finite elements, producing a surface mesh as shown in Figure 4. The dynamics are approximated over these finite elements and result in a system of algebraic equations. The system is then modelled using the assembled equations for the finite elements and solutions are approximated via the calculus of variations and minimising an associated error function. Producing AFM images requires the calculation of contours of constant indentation force. Using FEM, the sample surface and probe tip geometry are recreated, and individual indentations across the sample are simulated. This provides 4-dimensional arrays of indenter position and corresponding indentation force. From this, contours of constant force can be used to return the surface contour.

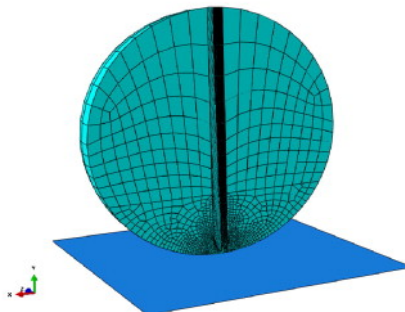


Figure 4: Graphic of FEM mesh for a simulation of sphere indentation by Zheng *et al.*³²

Our implementation of FEM utilises the commercial engineering software ABAQUS. However, as ABAQUS is an engineering-focused software and simulating biological AFM imaging is a novel application for ABAQUS, initial tests verified its viability. The accuracy of ABAQUS was evaluated through tests that focused on elastic indentation, performed on both elastic half-spaces with varying depths and elastic spheres with varying radii. These tests are outlined in Section 2.2. Following these initial simulations, a FEM approach was applied to produce simulations of the AFM raster-scanning dynamic, outlined in Section 2.3. These simulations were used to analyse the compression of a simple hemisphere and periodic surfaces (Section 2.4). Finally, a FEM approach was applied to simulate the AFM appearance of simple biomolecules, outlined in Section 2.3.3.

2 Methodology

2.1 ABAQUS Finite Element Analysis

To provide accessible simulations of AFM imaging, our implementation of ABAQUS utilised Python scripts to produce simulations (see Appendix ??). An ABAQUS model defines seven basic modules (shown in Figure 5): parts, properties, assembly, interactions, steps, loads/boundary conditions, and mesh. These moduli are defined within the Python code using predefined variables for the simulations, with geometric dimensions defined in nm and forces as pN. From this, a Python submission script is created and run by ABAQUS software. A brief outline of ABAQUS modelling follows.

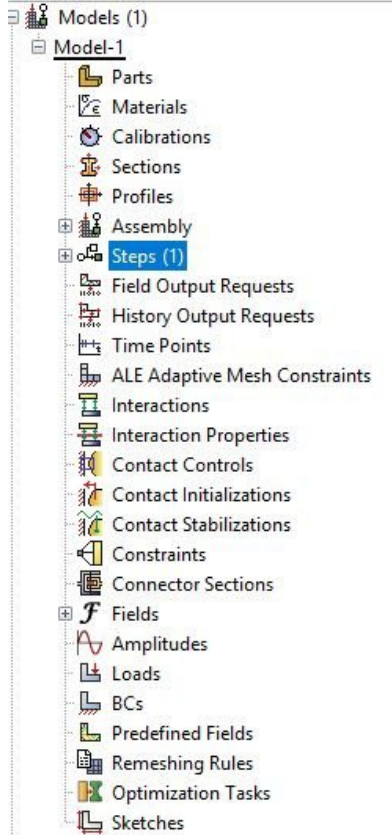


Figure 5: Display of model modules within ABAQUS GUI

The geometry of our simulation is the foundation of a model and is built as parts in the Parts module. Parts are formed from two-dimensional sketches that form a features profile. These profiles can be extruded, revolved, or swept to create part geometry or used directly to form a planar or axisymmetric part. Parts can be deformable, discrete rigid, analytical rigid, or Eulerian. The material properties and distribution for individual parts or sections of parts are set using the Properties module. The individual parts can then be joined and arranged in the Assembly module to create an assembly instance of the parts (known as part instances).

The behaviour of the part instances are defined in the interaction module, and various loads and boundary conditions can be applied to the part instances within the Load module. The Mesh module then allows the geometry to be coarse-grained and the surface subdivided into small, discrete finite elements. The steps module defines the sequence of one or more analysis steps and the increments of the analysis at which dynamics are propagated. The steps track the changes in the loading and boundary conditions of the model. The model can then be submitted, and the ABAQUS software runs the Finite Element Analysis.

2.2 Verification of Contact Models

Applying ABAQUS to assessing simple contact models of indentation provides a robust validation of the FEM approach. Three types of indenters were used for the simulations: conical, spherical, and spherically-capped conical. The behaviour of each indenter was characterized and compared with the theoretical indentation models: Hertz³³ and Dimitriadis³⁴ for spherical indenters, and Sneddon²⁷ for conical indenters (Details of the models are shown in the Appendix B). The simulations focused on the elastic indentation of both elastic half-spaces/planes of varying depths and elastic spheres of varying radii. For computational efficiency, asymmetric models centered around the indentation axis (y-axis) were used, as shown in Figure 6. Indenters were modelled as rigid (incompressible) parts restricted to the y-direction. The elastic half-spaces were fixed at the base, while the elastic spheres had a fixed, rigid base beneath them. The model surfaces were simulated as homogeneous, isotropic elastic materials with Young's modulus and Poisson ratio of 1000KPa and 0.3, respectively. These values were chosen as they are typical biomolecule values, and as such, dimensions were given in nm and pN (although somewhat arbitrary as analysis is dimensionless).

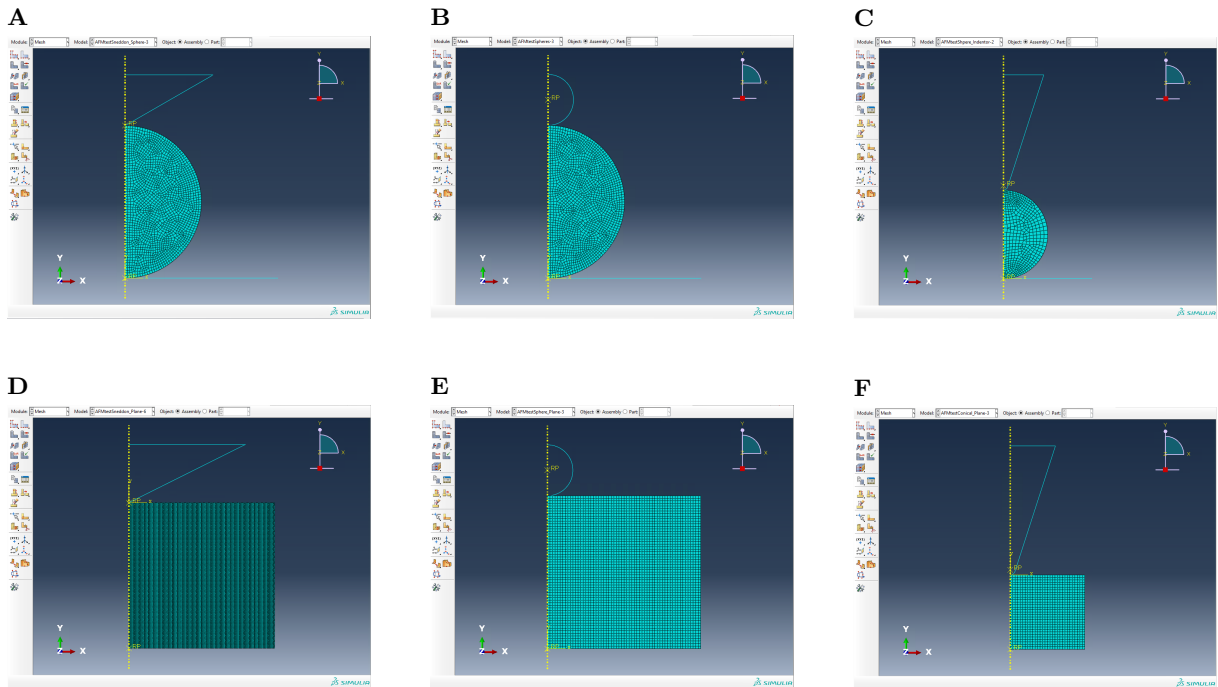


Figure 6: ABAQUS model assembly from elastic indentation tests. Elastic half-spaces were modelled asymmetrically using rectangles. Elastic spheres were modelled using semi-circles with a rigid base beneath. Models include (A) Conical indentation of an elastic sphere. (B) Spherical indentation of an elastic sphere. (C) Spherically-capped conical indentation of an elastic sphere. (D) Conical indentation of an elastic half-space. (E) Spherical indentation of elastic half-space. (F) Spherically-capped conical indentation of an elastic half-space.

The contact was modelled as a "surface-to-surface" type with "hard" (nonadhesive) properties in the normal direction and "rough" (non-slip) Coulomb friction in the tangential direction. Vertical force and indentation data was sampled via reference points at the centre of the indenter. As it is a rigid part, ABAQUS maps the forces and displacement of the surface of the part to the reference point. For elastic spheres, Double Contact Models^{35,36} were required to account for more complex dynamics discussed in the results. Simulations were quasi-static computations using an implicit algorithm and approximately 30000 tetrahedral (R3D10) elements. The simulation data was exported to Python and `scipy.curve_fit` module was used to fit the desired contact model. Example scripts in Appendix ??.

2.3 Simulation of AFM Imaging

2.3.1 General Scan Dynamics for Imaging

Following the application of FEM to single indentations, similar simulations were created to extend to AFM imaging. Independent ABAQUS simulations were produced in which individual indentations at positions across the surface's domain replicate the dynamics of an AFM raster-scan. Our AFM simulation subdivides the XY domain of the geometry into bins to produce the scan positions. The initial vertical heights of the indenter are then calculated at each position. Next, the independent ABAQUS simulations for the indentation at each position are produced, and corresponding vertical forces and displacements are extracted. This provided a four-dimensional array of indenter positions and corresponding force over the surface. Subsequently, computation of the contours for a given reference force produces the final AFM images shown in Figure 7. This methodology is computationally efficient as it utilises the initial heights computed from hard-sphere contact, resulting in the indentation data being consistently calculated to the same depth across the entire surface. This is as the hard-sphere contact represents the tangent points of the two surfaces' across the scan.

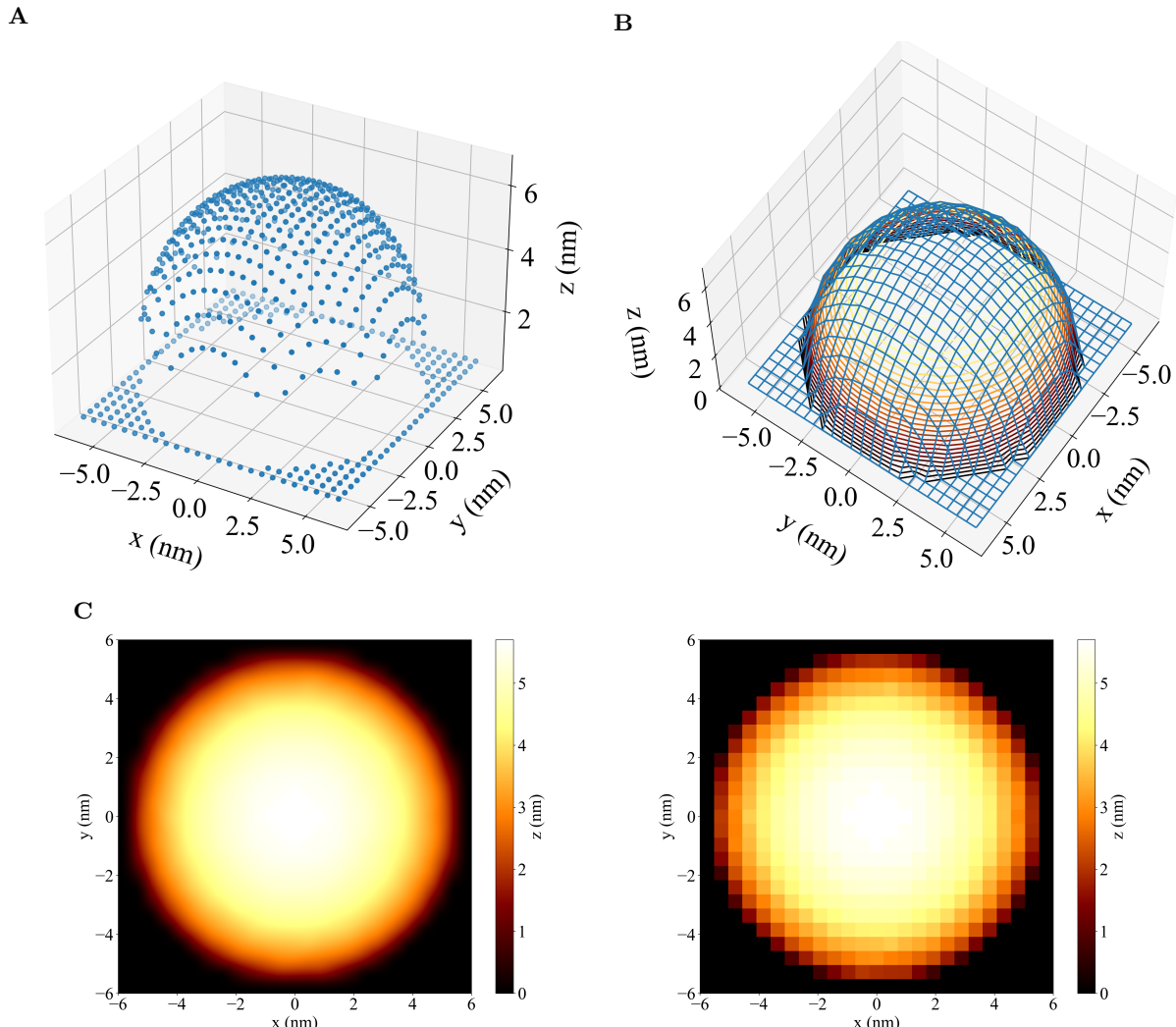


Figure 7: Plots for simulated AFM image on a hemisphere of radius $r=5\text{nm}$. $E = 1000\text{KPa}$, $\nu = 0.3$, and scan bins of 0.5nm . (A) Vertical initial scan positions for hemisphere. (B) Three-dimensional plot of force contours for 100pN for simulated AFM image. (C) Simulated 2D heatmap AFM image for 100pN force. Left: Interpolation. Right: Raw data

2.3.2 Image Processing and Interpolation

The pseudo-AFM images are produced from two-dimensional arrays of surface heights over the XY grid of scan positions. These heights map the surface contour of equal force over the scan. These contours are calculated from the indentation depth and force arrays produced by the ABAQUS/FEM simulations. For a given threshold/ reference force, the corresponding depths are found using a list comprehension (see Figure 8). The list comprehension iterates over the force data for each scan position and compares it with the reference force. The index for the value equal or greater than the reference force is found and the corresponding depth is stored. This is used to calculate the surface heights. If no values in the force array for a scan position are greater than the reference force, the function sets the corresponding contour value to the maximum indented depth. The contour data is then reshaped into the 2D grid representing the scan positions. Subsequently, the Matplotlib imshow function is used to produce the visualisation with a Colormap to illustrate the variation in surface heights. Normalisation of the colourmaps applies either linear scaling over the domain or power normalisation depending on detail contrast. Moreover, to increase pixel density images are interpolated using Matplotlib imshow functions in-built bicubic interpolation.

```

1  def ForceContours(U2, RF, forceRef, scanPos, baseDims, binSize):
2      ...
3      Function to calculate contours/z heights of constant force in simulation data for given threshold force.
4
5      Parameters:
6          U2 (arr) - Array of indentors z displacement over scan position
7          RF (arr) - Array of reaction force on indentor reference point
8          forceRef (float) - Threshold force to evaluate indentation contours at (pN)
9          scanPos (arr) - Array of coordinates [x,y,z] of scan positions to image biomolecule
10         baseDims (list) - Geometric parameters for defining base/ substrate structure [width, height, depth]
11         binSize (float) - Width of bins that subdivide xy domain during raster scanning/ spacing of the positions sampled over
12     Return:
13         X (arr) - 2D array of x coordinates over grid positions
14         Y (arr) - 2D array of y coordinates over grid positions
15         Z (arr) - 2D array of z coordinates of force contour over grid positions
16     ...
17
18     # Initialise dimensional variables
19     xNum = int(baseDims[0]/binSize)+1
20     yNum = int(baseDims[1]/binSize)+1
21
22     # Initialise contour array
23     forceContour = np.zeros(len(RF))
24
25     # Loop over each reaction force array, i.e. each scan positions
26     for i in range(len(RF)):
27
28         # If maximum force at this position is greater than Reference force
29         if np.max(RF[i]) > forceRef:
30             # Return index of force threshold and store related depth
31             j = [k for k, v in enumerate(RF[i]) if v > forceRef][0]
32
33             # Set surface height for reference height
34             forceContour[i] = scanPos[i,2] + U2[i,j]
35
36             # If no value above threshold set value at bottom height
37             else:
38                 forceContour[i] = scanPos[i,2] + U2[i,-1]
39
40     # Format x,y,z position for force contour
41     X = scanPos.reshape(yNum, xNum, 3)[ :, :, 0]
42     Y = scanPos.reshape(yNum, xNum, 3)[ :, :, 1]
43     Z = forceContour.reshape(yNum, xNum)
44
45     return X, Y, Z

```

Figure 8: Code Snippet showing the calculation of force contours for AFM image. For a given threshold/ reference force, the corresponding depths are used to calculate the surface heights over the scan positions.

2.3.3 Application to Biomolecules

The application of these dynamics to biomolecules requires some simple modifications. Biological structures are produced using Protein Data Bank (PDB) files that specify the constituent atoms of a biomolecule and the corresponding coordinates. As the simplest approach, the biomolecule is modelled as an elastic material produced from the assembly of spheres (with van der Waals radius) of the individual atoms. The structure is assumed to be a continuous, homogeneous and isotropic material, with a typical biological Young's Modulus and Poisson ratio of 1000KPa and

0.3, respectively. The molecule is partially embedded in a rigid base/ substrate, and the scan positions are then calculated over the domain of the base. The embedded portion simulates a soft molecule absorbed onto a solid support and the molecule is then fixed at its base using boundary conditions. The AFM probe tip is modelled as a rigid capped conical indenter where the indentation is non-slip and without adhesion. The contact is modelled as "surface to surface" type, with the properties of hard contact in the normal direction and "frictionless" in the tangential direction to ensure no slip and no adhesion. Indentation data from the indenter is mapped and sampled via reference points at the centre. The computations were quasi-static with an implicit algorithm and using R3D10 tetrahedral elements (generally greater than 100,000). The elastic constitutive relations are integrated with the main body of the Abaqus code.

The initial scan positions must be calculated numerically as PDBs only provide atom positions, not surface structure. The XY scan positions are produced by creating a rectangular grid of positions over the base, each separated by a predefined bin size. The heights at each position are calculated by setting the tip above the sample and calculating the minimum vertical distance between the tip and the molecule's surface (corresponding to the tangent point of the two surface's). Figure 9 illustrates the calculations made by the code. For each scan position, a loop is used to calculate the radial distances to the atoms in the biomolecule (shown as $R_{Interact}$ in Figure 9). If the atom lies within the indenter's boundary ($R_{Boundary}$), the atom and indenter could interact. Therefore, the vertical distances between the surface of the indenter and the "interacting atoms" of the molecule are computed. This produces an array of "dz" values which represents all differences in height between the tip and portion of molecule located within the boundary of the indenter. As illustrated in Figure 9, the minimum of these values gives the vertical distance corresponding to the position where the tip is in tangential contact. Subsequently, using this minimum dz value the tangent points for a scan location can be calculated. Repeating this for all scan locations provides an array of coordinates [x,y,z] of scan positions. For computational efficiency, this can be clipped to only include positions where the tip and molecule interact.

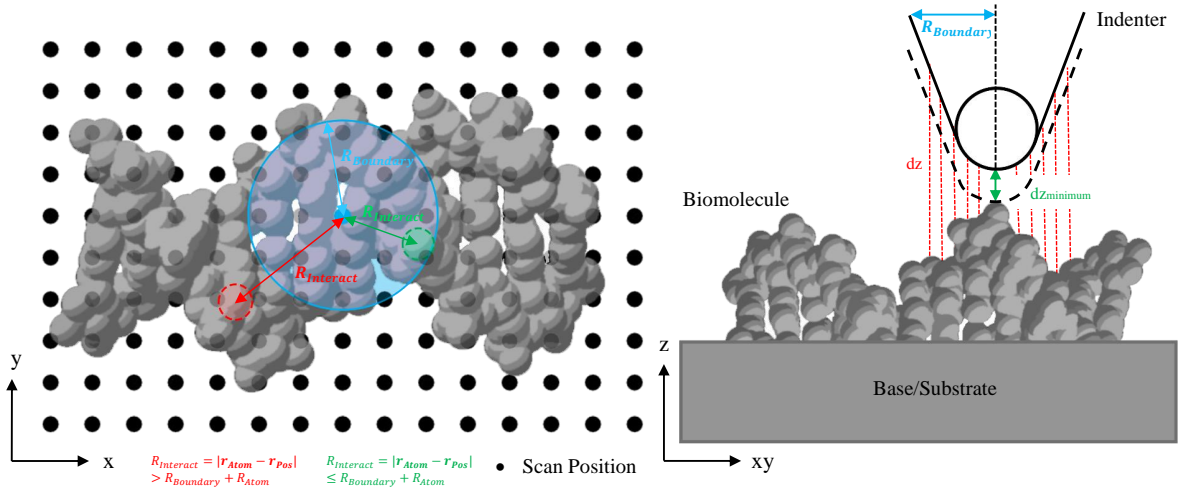


Figure 9: Schematic diagrams illustrating the calculation of initial scan heights in AFM code. Left: Illustrates the calculation atoms on the surface within the indenter's boundary. Black dots represent the XY grid of scan positions. The calculation is restricted to the XY plane in which only atoms inside the radial extent of the indenter, $R_{Boundary}$ (blue), are calculated. The red atom represents an atom outside the extent and thus is omitted, as opposed to the green atom, which is included. Right: Illustrates the calculation of heights for each given position. An array of all distances (dz) between the indenter and molecule surfaces are calculated (red). The minima of these distances thus give the translation distance to place the indenter in tangential contact.

An outline of the simulation script is shown in Figure 10. The code has three main phases: In

the preprocessing phase, the desired PDB file is imported via the PDB function and used to process the biomolecule's structure in the MolecularStructure function. Subsequently, the base and indenter geometry is calculated, and the ScanGeometry function determines scan positions for the simulation. These variables and other predefined simulation variables are exported to CSV files using the ExportVariables function. Finally, the CSV files and the ABAQUS scripts are transferred to the remote server where the simulations are carried out. There are 3 ABAQUS scripts run in the submission phase. First, the SurfaceModel and RasterScan scripts are run sequentially using the RemoteCommand function. These scripts produce the ABAQUS surface model and input files for simulations at each scan position. Next, the BatchSubmission function creates a script to run the input files sequentially on the remote server. Once the simulations are complete, the data is stored in ODB files. Running the ODBAnalysis script extracts the indentation data and exports it to CSV files. Once completed, the simulation data can be transferred back to the local machine, where it is processed. In the postprocessing phase, the Data Processing function extracts data from the CSV files and formats the data to include all scan positions. The ForceContour function subsequently calculates the surface heights for a given reference force. Finally, this is plotted in an AFM image using ContourPlot function. (See Appendix ?? for complete code).

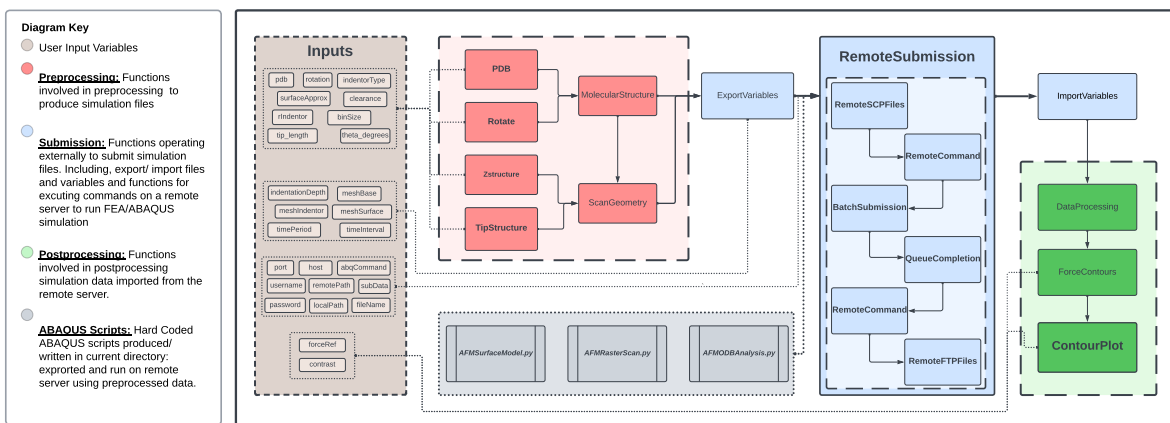


Figure 10: Flow diagram outline code functions and processing

2.4 Analysis of Surface Compression

2.4.1 Simulation Dynamics

This finite element approach can be extended to provide quantitative analysis of the indentation of surface features in AFM imaging. Of interest is the simulation of spherical and simple periodic structures. Within a natural setting, a hemisphere provides an analogy for various structures, and the deformation of a periodic structure provides a comparison for the analysis of DNA imaging. These structures were modelled as three-dimensional elastic parts in ABAQUS, with simulations focused on the compression produced from a single scan along the centre axis of the structures. Surfaces are assumed to be homogeneous and isotropic with a relative Young's modulus and Poisson ratio comparable to biomolecules as before. Indentations were simulated with a rigid, spherically capped conical indenter and "surface to surface" type contact. The contact was set as "hard", nonadhesive contact in the normal direction and "rough" Coulomb friction (non-slip) in the tangential direction. Boundary conditions fix the base of the structure, and vertical force and indentation data are mapped and sampled via reference points at the centre of the indenter. The simulations produced 2D force and indentation data over the central axis. The radial compression of spherical samples and the distortion in periodic structures are analysed as functions of the indentation force and the contact radius. The scan geometries are shown in Figure 11, and the following section details the techniques used to analyse the data. Example scripts are viewable in Appendix ??.

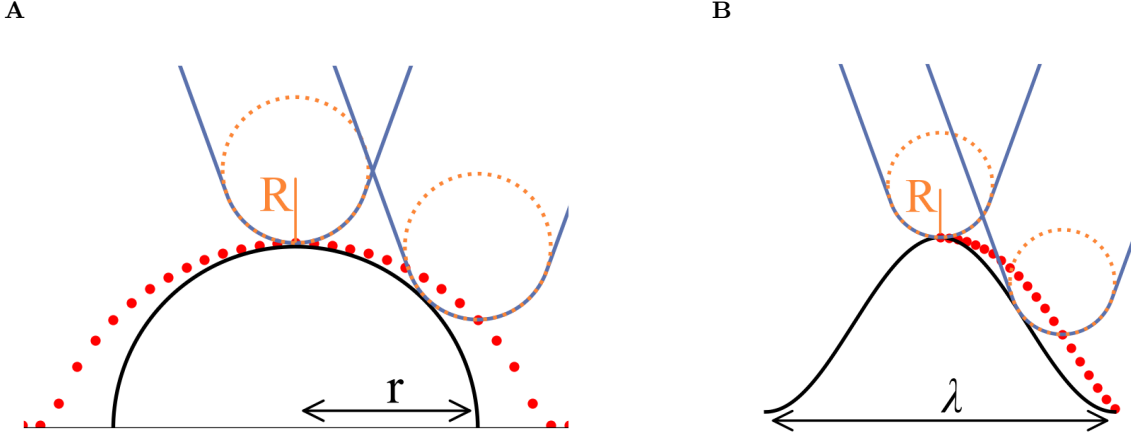


Figure 11: (A) Geometry of scan along the central axis of a hemisphere. Three-dimensional geometry is produced by rotating the indenter and semi-circle around the central z-axis. The hemisphere is shown in black with a radius r . Indenter geometry is shown in blue with a circular tip of radius R in orange. Red points indicate initial scan positions (Hard sphere contact points). (B) The geometry of the scan along the central axis of a plane wave structure for a half wavelength. Three-dimensional geometry is produced by rotating the indenter around the central z-axis and extruding the wave in the out-plane direction. Wave is shown in black with wavelength λ . Indenter geometry is shown in blue with a circular tip of radius R in orange. Red points indicate initial scan positions (Hard sphere contact points).

2.4.2 Heat Map and Force Contours

A heat map of the force over the scan domain was produced by processing data from indentation simulations. The heat map are produced by iterating over the course-grained x and z coordinates of the scan and mapping the corresponding force at each position into a 2D grid of the scan domain. This provides a grid of the force across a cross-section of the surface. A mask is used to exclude positions with no indentation data. Similarly, the force contours are calculated by iterating over each x coordinate and evaluating the force. The code finds the index for the value equal to the reference force and stores the corresponding XZ position. If the maximum force is below the threshold, the code masks that value in the contour array.

2.4.3 Full Width Half Maxima

Full-width half maximum (FWHM) measures the width of a peak in a spectrum at half of its maximum amplitude. FWHM characterise the resolution and peak shape of the contour. In Python, calculating the FWHM for the contour data is achieved by fitting a cubic spline to the contour data using the `scipy.interpolate` module. Once the spline is fitted, the FWHM can be calculated from the roots at half the maximum value. Finding the roots uses the `UnivariateSpline.roots` `scipy` function. This approach is advantageous because it provides a smooth representation of the data, which can help analyse noisy data sets.

2.4.4 Fourier Analysis

Fourier series express a periodic function as an infinite sum of sine and cosine waves, each modulated by an individual amplitude and frequency. Fitting data to a Fourier series allows for analysis of the spatial resolution of the contours produced. In Python, fitting data to a Fourier series is achieved using an explicit function for the series and `scipy.optimize curve_fit` function. Data used to fit the series was extrapolated from a tight spline of the raw contour data. This is used to ensure the smoothness of the fit and avoid overfitting due to a reduced number of data points. The `curve_fit` function returns the optimised coefficients and the covariance matrix. As the surface and contours are symmetric functions, Fourier analysis only requires the cosine terms given by,

$$F(x) \approx \sum_{n=0}^{\infty} A_n \cos\left(\frac{2\pi n t}{T}\right) \quad (1)$$

2.4.5 Volume Analysis

Volume analysis provides a quantitative metric for compression and distortion at varying indentation forces. Volume was calculated from splines fitted to the force contours using the Scipy UnivariateSplines class. This class provides an integral method that can be used to calculate the definite integral of the spline over a specified interval. The integral method uses numerical integration techniques to approximate the area under the curve, which can then be interpreted as the volume.

2.4.6 Youngs Modulus

The variation of fitted Young's Modulus over the scan positions illustrates the perceived elastic response of the surface. We use the same procedure used for contact models to fit the Hertz model in Python. Using the Scipy curve_fit function, the Hertz model is fitted for the indentation data at each scan position. Young's modulus is used as the fitting parameter—this returns the variation of fitted Young's modulus over the scan positions.

3 Results

3.1 FEM Verification of Contact Models

3.1.1 Elastic Half-space

The indentation of a spherical indenter into an elastic half-space is the simplest model to analyse; here, both the Hertz³³ and Dimitriadiis models³⁴ are compared (Appendix B.1 and Appendix B.3). This is an important test, as the indentation in AFM experiments with blunt tips can be assumed to be spherical^{37,38}. Similarly, analysing conical indenters into an elastic half-space is an important comparison for AFM experiments with sharp tips. Here the Sneddon model²⁷ (Appendix B.4) is compared with the Hertz model. Moreover, the same analysis is applied to a spherically capped conical indenter. Illustrations of the indentation are shown in Figure 12B .

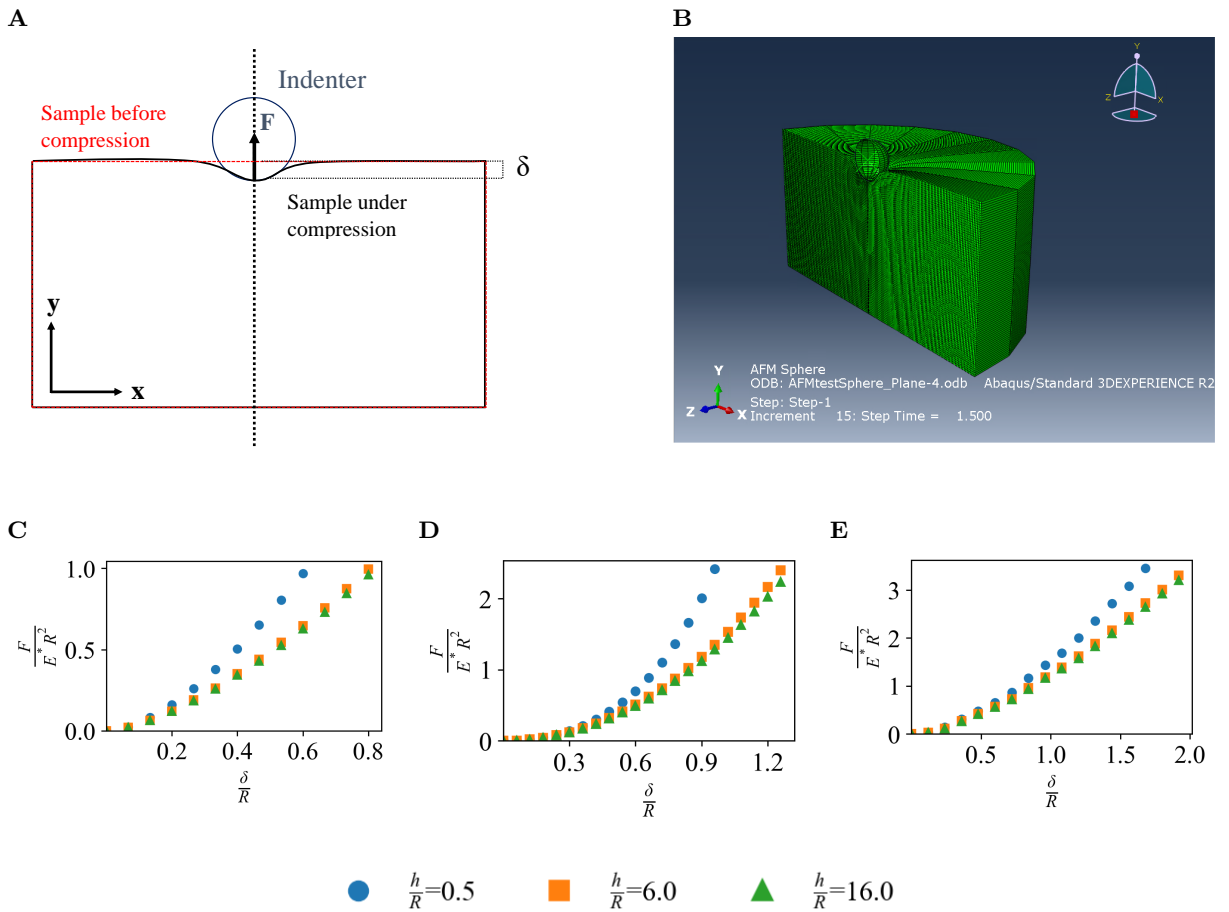


Figure 12: (A) Illustration of contact experienced by elastic half-space for indentation depth δ , and force, F . (B) Visualisation from GUI for the sphere-plane indentation where the asymmetric model is rotated 180 degrees around the central axis. (C)-(E) Force curves for indentation into an elastic half-space with varying plane depth and radius, h . Given in dimensionless units of force ($\frac{F}{E^* R^2}$) and indentation (δ/R). (C) Force curve for spherical indenter. (D) Force curve for conical indenter with half-angle of $\alpha = 60^\circ$. (E) Force curve for capped conical indenter with a half-angle of $\alpha = 20^\circ$. To normalise conical indenter data R is set as max contact radius $R = \delta_{max} \tan(\alpha)$.

As shown in Figure 12, these simulations gave the characteristic force curves for each indenter. For greater applicability, the simulation data is analysed in dimensionless units of force and relative indentation, which are scaled using the Hertz contact equation (given in Appendix B.1). The conical indenter shows the most significant curvature in its force curve. This is because contact forces are distributed more over the spherical surfaces than the sharper tip. Therefore,

the conical indenter produces more prominent deformation for the same force.

In comparison, the capped conical indenter produced a curve with transitional behaviour around $\delta/R = 1$, which is expected as the indenter moves from the spherical portion to the conical. Moreover, as the surface size (h) increases, the area bounded by the curves decreases. As the area under the curve represents the elastic energy of indentation, this behaviour illustrates the increased energy required to compress smaller planes. This is because the indentation on smaller surfaces causes significant horizontal shear stress, and indentation to the same depth cause more extensive compression. Therefore, this effectively produces greater stiffness and elastic energy.

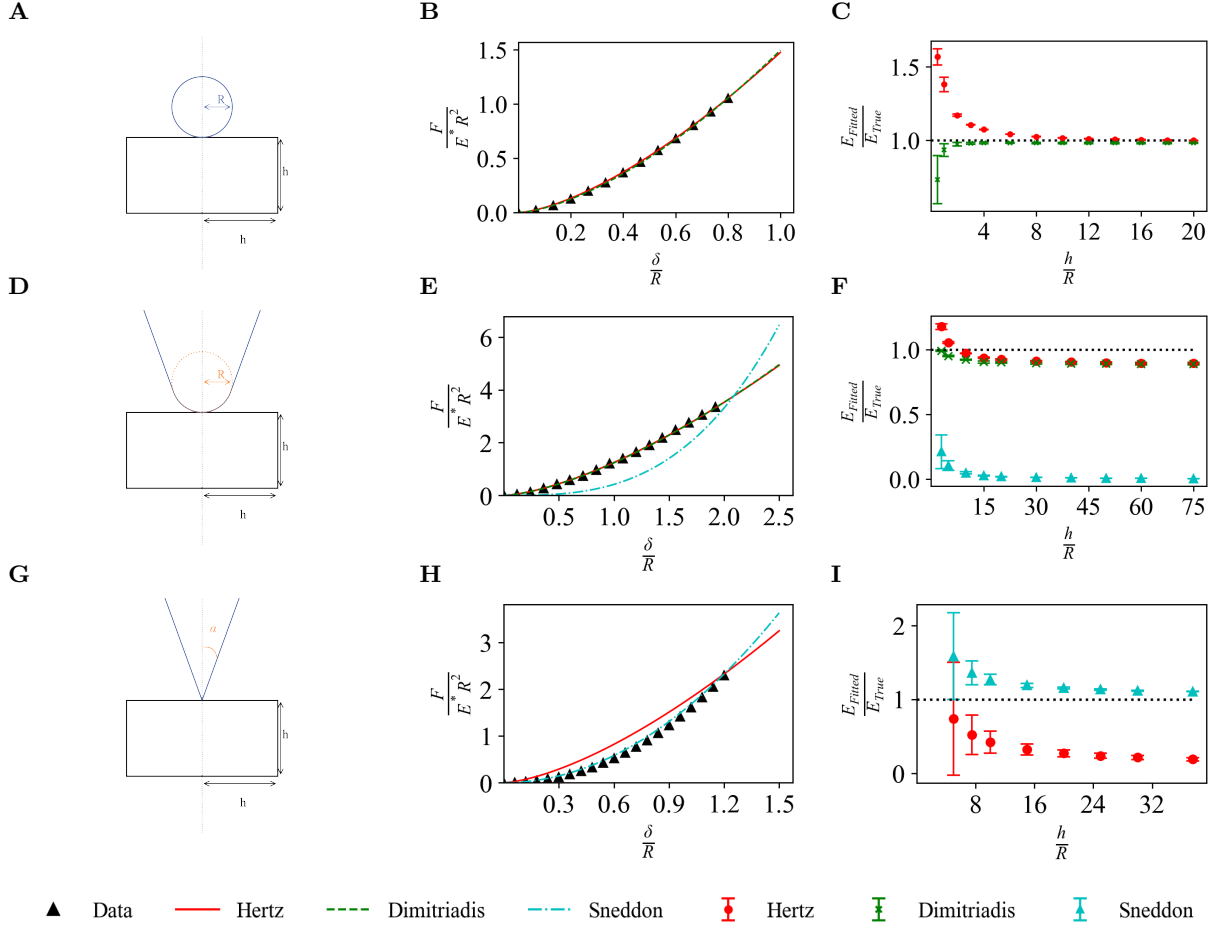


Figure 13: (A) Model assembly for spherical indentation of elastic half-space. (B) Plot for spherical indentation force curves fitted using the Hertz and Dimitriadiis models. (C) Young's Modulus variation for spherical indentation into elastic half-space. (D) Model assembly for spherically-capped conical indentation of an elastic half-space. (E) Plot for capped indentation force curves fitted using the Hertz, Dimitriadiis, and Sneddon models. (F) Young's Modulus variation for conical indentation into elastic half-space. (G) Model assembly for conical indentation of an elastic half-space. (H) Plot for conical indentation force curves fitted using the Hertz and Sneddon models. (I) Young's Modulus variation for conical indentation into elastic half-space. For conical indenter data normalisation $R = \delta_{max} \tan(\alpha)$.

Fitting the contact models to the simulated data for the spherical indenter, shown in Figure 13B, showed good adherence from both Hertz and Dimitriadiis models. Moreover, comparing the fitted Young's modulus for increasing surface geometry, in Figure 13C, shows both models converged on the expected Young's modulus, confirming the accuracy of the simulation dynamics. However, there was a significant divergence from the predicted Young's modulus at small surface geometry and a greater error in the fit. This behaviour is expected as the indenter is a comparable size to the surface at smaller surface dimensions. Therefore, the force is distributed over a larger portion of the surface and can cause buckling and shear forces as the plane bulges out. In addition, this

can create larger reaction forces at the base. Consequently, this creates deviation from the theoretical models along with the contradiction of the assumption of an elastic half-space with an infinite horizontal/vertical extent.

Similarly, for the capped conical indenter, the Hertz and Dimitriadiis model provided a much tighter fit to the data than the Sneddon model, which deviated as shown in Figure 13E . This indicates that the spherical behaviour dominates over the conical behaviour at these ranges. This qualitative behaviour is further reinforced by the variation of Young's modulus over surface depth/radius shown in Figure 13F . The Sneddon model converges on zero, indicating that the model diverges to a large extent and is a poor description of the indentation. In contrast, the Hertz and Dimitriadiis models converged closely on the expected Young's modulus. Some deviation is expected as the models are for a pure spherical indenter, whereas the conical section of the capped indenter causes variation in the contact.

Lastly, the Sneddon model produced an expected tight fit for the conical indenter, whereas Hertz was a poor fit. As expected, the Hertz model failed to converge upon the correct Young's Modulus and produced a large underfit because the model is for smaller spherical deformation. However, the Sneddon model converges to the true value. These results all provided the expected behaviours and confirmed the accuracy of ABAQUS. This provides the basis to be applied to simulations of AFM imaging.

3.1.2 Elastic Sphere

The analysis of the elastic sphere is more complex, as it necessitates accounting for the indentation between the indenter and the surface and the indentation between the surface and the base. As shown in Figure 14C , the simulations give the characteristic force curve for the indenter and, as before, as the radius of the surface increases, the bounded area decreases. However, from Figure 14D , it can be seen that sampling data at the base of the sphere shows the surface is compressed. However, due to the extremely small indentation, the Hertzian behaviour closely approximates a linear relationship at the base, exhibiting a response consistent with Hooke's Law.

Moreover, Figure 14 shows the indentation of the elastic sphere into the base. Indentation force is distributed between the reaction at the base and the indenter, and part of the perceived indentation depth is due to compression at the base. Therefore, corrected values for the indentation depth is calculated by subtracting the surface compression at its base from the indenter's displacement. Similarly, the corrected forces are the sum of the reaction forces. However, as this research focuses on AFM imaging, the fitted force and indentation data are produced from the indenter data alone, and compression is accounted for using "Double Contact" models^{35,36}(Appendix B.5).

For these simulations, the radius of the elastic sphere is varied to test the model's accuracy across varying curvature. Figure 15B shows the difference in the corrected and indenter data. Fitting the contact models to the spherical indenter's data produced tight adherence from the Hertz, Dimitriadiis, and Double Contact models. Similarly, for the capped conical indenter, shown in Figure 15E , the Hertz, Sneddon, and Double Contact models produced tight fits. In contrast, the Hertz model gave a poor fit for the conical indenter, while the Sneddon and Double Contact models produced tight fits.

Comparing the fitted Young's modulus variation over surface radius produced various convergent behaviours. The results indicate that the simple Hertzian model underestimates the elastic modulus as the data converged below the expected value for all simple contact models. In contrast, the double contact models converge to the actual value. This highlights the importance of the contribution of compression at the base of the sample. Considering only the indenter data reduces the force experienced by the indenter, reducing fitted Young's modulus.

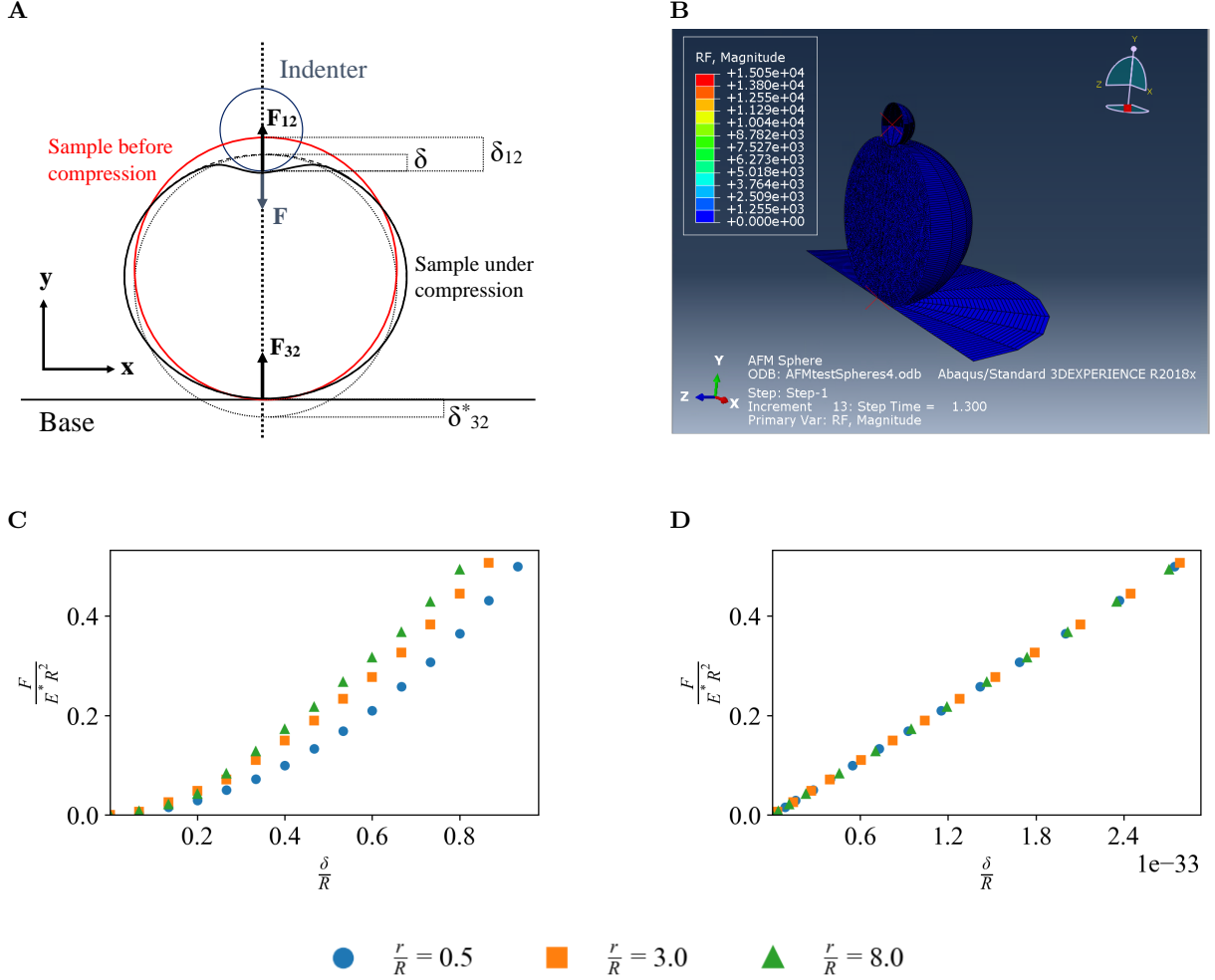


Figure 14: (A) Illustration of double contact experienced by spherical sample. For indentation δ , indenter displacement δ_{12} , surface compression δ^*_{32} , indentation force F , indenter reaction force F_{12} , and base reaction force F_{32} . (B) GUI visualisation for the sphere-sphere indentation where the asymmetric model is rotated 180 degrees around the central axis. (C) Force curve for spherical indentation δ/R into the elastic sphere of varying radius, r/R . (D) Force curve for compression of the surface into the base. Conical and capped indenter data is not shown, however, shows similar trends as before.

As shown in Figure 15C, the double contact models converged on the expected value for a spherical indenter. However, the error in the fit fluctuates as the surface radius increases. At small surface radii, excessive amounts of compression cause significant error and deviation from the theoretical models. The error decreases as the radius of the surface increases and compressive effects lessen; however, the error increases again at large surface radii as the geometry approximates an elastic half-space, and the double contact model is no longer valid. In contrast, errors in the Hertz and Dimitridias models decrease as the surface curvature decreases and the surface approximates an elastic half-space.

The Hertz model converged close to zero for the conical indenter shown in Figure 15I. This indicates that the model diverges to large extents, which is expected as the Hertz model is for spherical indenters and an elastic half-space. On the other hand, the Sneddon model for the conical indenter converged to around 0.5. As discussed before, this is due to the compression of the sample, which reduced the reaction force at the tip. In contrast, applying a novel formulation of the Double Contact model for conical indenters (shown in Appendix B.7) produces a tight fit to the actual value across all surface radii.

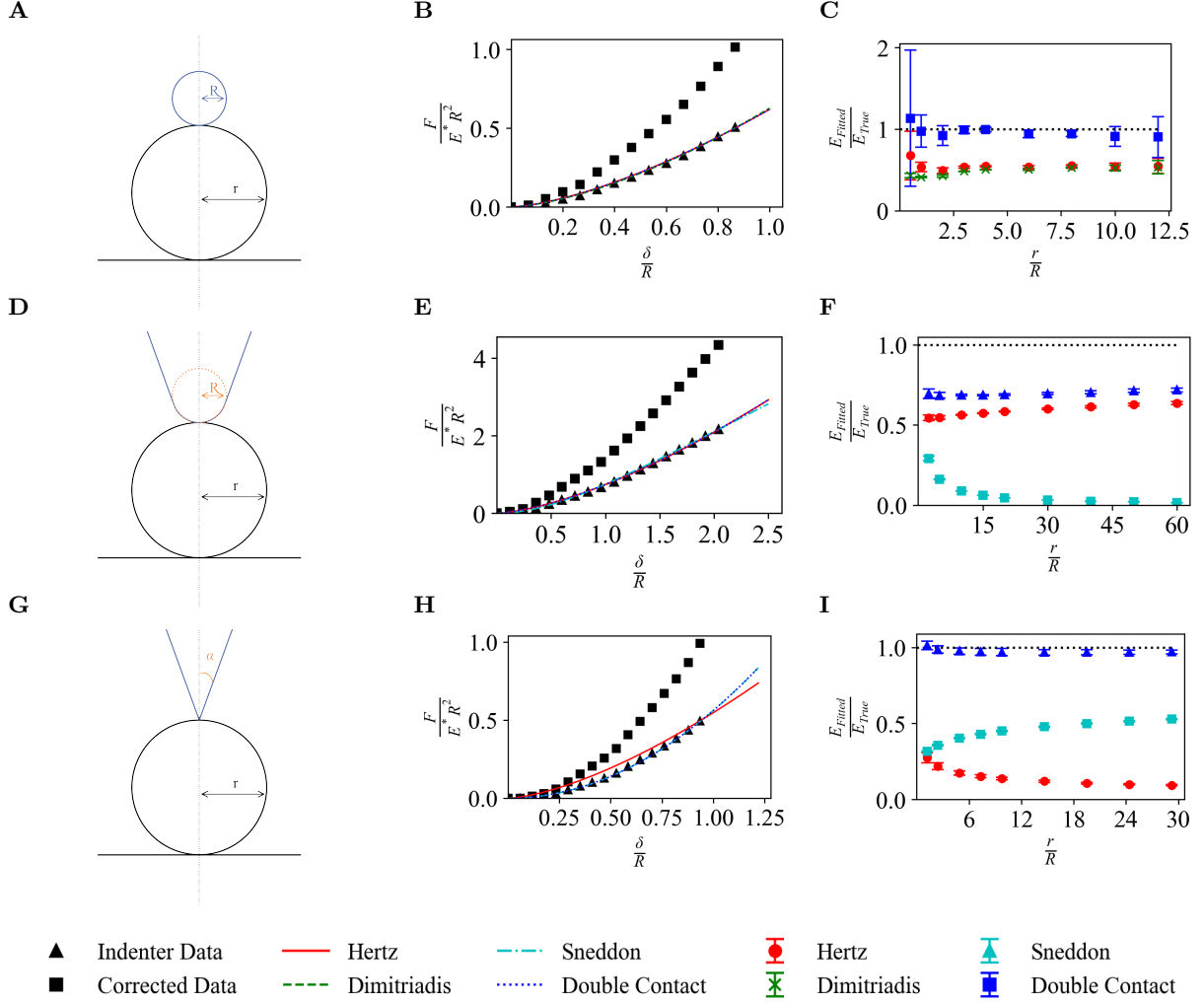


Figure 15: (A) Model assembly for spherical indentation of the elastic sphere. (B) Plot for spherical indentation force curves fitted using the Hertz, Dimitriadis, and Double Contact models. (C) Youngs Modulus variation for spherical indentation into an elastic sphere. (D) Model assembly for spherically-capped conical indentation of an elastic sphere. (E) Plot for capped indentation force curves fitted using the Hertz, Sneddon, and Double Contact models. (F) Youngs Modulus variation for capped conical indentation into an elastic sphere. (G) Model assembly for conical indentation of an elastic sphere. (H) Plot for conical indentation force curves fitted using the Hertz, Sneddon, and Double Contact models. (I) Youngs Modulus variation for conical indentation into an elastic sphere. For conical indenter data normalisation, $R = \delta_{max} \tan(\alpha)$. Conical and capped indenters have the same dimensions as used in half-space simulations.

In comparison, for the capped indenter, the Double Contact model converged around 0.75. This offset is expected because the non-spherical portion of the indenter produces less curvature and deviation from the theoretical model. Similarly, the deviation produced by compression at the base leads to a similar convergence in the Hertz model. In comparison, the Sneddon model shows poor fit as it converges to 0. This indicates that the spherical indentation is dominant at these depths. Overall, these results further validated our ABAQUS modelling.

3.2 FEM Applied to Compression Simulation

The finite element approach presented in this research can be extended to analyse the compression of surfaces in AFM imaging. Spherical and periodic structures provide the simplest structures to consider. These structures were modelled as three-dimensional, homogeneous elastic parts with elastic modulus and Poisson ratio comparable to biomolecules. The simulations focused on the compression produced when scanning along the centre axis of the structures, generating 2D force and indentation data over the restricted central axis. Subsequently, the radial compression of spherical samples and distortion in periodic structures are analysed as a function of the indentation force. This elucidates the responses and characteristics produced in the surfaces under AFM imaging and the apparent appearance of the structure.

3.2.1 Analysis of Hemisphere Structure

As presented in Figure 17, the hemisphere simulations provided 2D heat maps of the indentation force across a surface cross-section. This displays the force experienced at each depth along the scan line. The raw data from the simulation, shown in 16A , produces a course-grained distribution of indentation force over the scan. Using interpolation methods detailed in Section 2.4, the data can be smoothed to produce a continuous distribution shown in Figure 16B . From the raw data, contours of constant force can be extracted to analyse the perceived shape at varying forces as presented in Figure 16C .

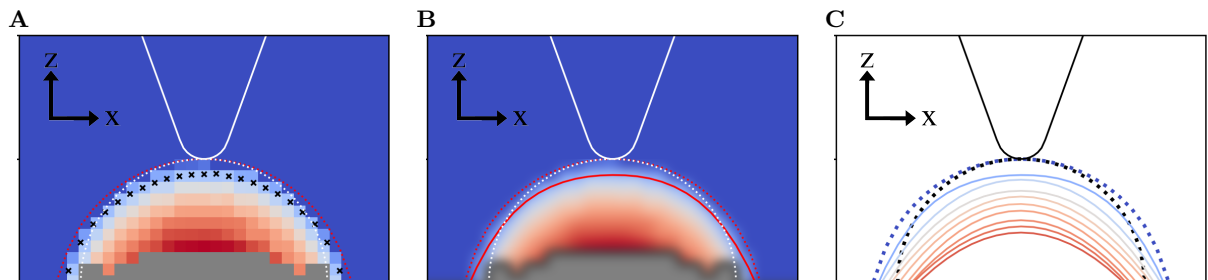


Figure 16: Illustrations of data produced from compression simulations for indenter $R/r = 0.2$. (A) Raw two-dimensional heat map of indentation force over the scanning axis for the hemisphere structure. Including the points of constant force, $\frac{F}{E^*R^2} = 0.227$, shown as black crosses. These are points used to produce the force contours. The indenter is solid white, and the surface is dotted white. Points of zero force/ hard sphere contact is shown in dotted red. (B) Interpolated two-dimensional heat map of indentation force over the scanning axis for the hemisphere structure. Including overlayed contour of constant force, $\frac{F}{E^*R^2} = 0.227$, shown in solid red. The indenter is solid white, and the surface is dotted white. Points of zero force/ hard sphere contact is shown in dotted red. (C) Two-dimensional plot of force contours for varying indentation/ reference forces over the scanning axis of the hemisphere structure. Force shown varies within the limit of $0.227 < \frac{F}{E^*R^2} < 3.867$. The indenter and surface are black, with the initial zero force/ hard sphere boundary in dashed blue.

Analysis of the compression, shown in Figure 17B and 17C , revealed that increasing the indenter-to-surface ratio results in lower indentation forces. As the surface-indenter ratio/contact radius increases, the forces are spread over a larger area, resulting in less deformation for the same force. Combined with greater tip convolution, this increases the broadening of the surface's appearance. This is reflected in fitted Young's modulus as shown in Figure 17D . As indentation force, and therefore fitted Young's modulus, varies as a function of the contact radius, the variation in Young's modulus over the scan position emulates the scan geometry. Therefore, larger indenters produce a flatter fitted Young's modulus. This highlights that increasing the indenter-surface ratio is analogous to scanning a surface with greater Young's modulus. Physically, this corresponds to greater effective stiffness experienced at larger indenter-surface ratios, as forces are distributed over a larger surface area and larger forces are required for equivalent compression. Interestingly, due to the flattening produced, larger indenter-surface ratios provide

a greater estimation of the true Young's modulus over the scan positions.

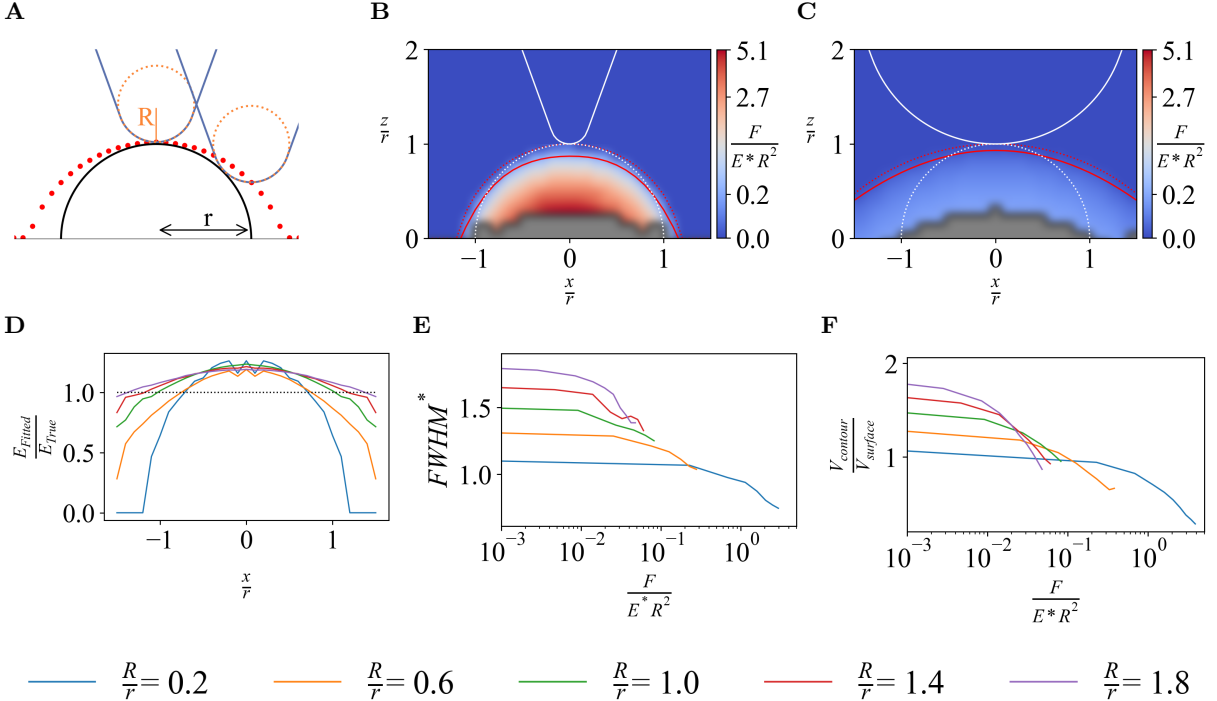


Figure 17: (A) Geometry of scan along the central axis of a hemisphere. Three-dimensional geometry is produced by rotating the indenter and semi-circle around the central z-axis. The hemisphere is shown in black with a radius r . Indenter geometry is shown in blue, with the circular tip of radius R in orange. Red points indicate initial scan positions (Hard sphere contact points). (B) Interpolated two-dimensional heat map of indentation force over the scanning axis for hemisphere structure with indenter $R/r = 0.2$. Including overlaid contour of constant force, $\frac{F}{E^* R^2} = 0.227$, shown in solid red. The indenter is solid white, and the surface is dotted white. Points of zero force/ hard sphere contact is shown in dotted red. (C) Interpolated two-dimensional heat map of indentation force over the scanning axis for hemisphere structure with indenter $R/r = 1.4$. Including overlaid contour of constant force, $\frac{F}{E^* R^2} = 0.227$, shown in solid red. The indenter is solid white, and the surface is dotted white. Points of zero force/ hard sphere contact is shown in dotted red. (D) Fitted Young's modulus over scan positions for each indenter radius (R/r). (E) Relative FWHM of the contour divided by FWHM of true geometry ($FWHM^* = \frac{FWHM}{FWHM_{True}}$) variation over contour force for each indenter radius(R/r). (F) Volume variation over contour force in spherical structures for each indenter radius(R/r).

The Full Width Half Maxima (FWHM) provides information about the spread of the contour. The FWHM value reflects the surface's compression and is used as an indicator flattening of the contour. As shown in Figure 17E , FWHM decreases asymptotically as the indentation force decreases. As the force decreases to zero, each indenter converges on the corresponding FWHM of the hard sphere boundary. Conversely, as the force increases, the sample is indented to greater depth producing tighter, compressed force contours and narrowing the surface's appearance. For larger indenters, this produces force contours with FWHM closer to the true FWHM. However, this does not directly show that the higher force provides a more accurate recreation of the sample surface. The compression of the sample can produce elliptical contours that do not represent the hemisphere yet share the same FWHM. For a smaller indenter, which approximates the surface geometry more closely at low force, the increased compression at higher forces produces an FWHM that diverges from the true surface FWHM. Furthermore, the nonlinear behaviour of the FWHM highlights that the compression producing the force contours is not a simple linear relationship.

Furthermore, the apparent volume can quantify compression over various contour forces. As shown in Figure 17F , the volume decreases exponentially as the indentation force increases. This further validates the behaviour shown by the FWHM. As the indentation force increases,

greater compression is produced, reducing the apparent appearance. In addition, as indenter size decreases, larger forces are required to achieve the same relative decrease in volume. This is expected as smaller indenters have smaller contact areas; therefore, larger forces are required to compress the sample to the same extent.

Overall, this analysis highlights three main characteristics of the hemisphere under compression. First, the Youngs modulus shows the dependence of elastic response/behaviour on the contact radius and tip convolution. The FWHM is an important analysis to demonstrate the nonlinear compression and widening of the perceived surface. Finally, the volume highlights that the larger indenters/contact areas require larger forces to compress the sample to the same extent as smaller indenters.

3.2.2 Analysis of a Simple Periodic Structure

Expanding upon the simulation of a hemisphere, next, we analyse the deformation of a periodic structure that provides a comparison for the analysis of DNA imaging. As presented in Figure 18, the simulations produced 2D heat maps of the indentation force across the cross-section of the surface. Comparison of cross sections for different indenter ratios, shown in Figure 19B and Figure 19C , shows that increasing indenter-to-surface ratios produces lower indentation forces. As with the hemisphere, due to the large contact radius, the forces are distributed over a large area; consequently, the compression is smaller for the same force. Moreover, evaluating the variation of the fitted Young's modulus over the scan positions, shown in Figure 19D , highlights the relation between elastic response/ force and the contact area. Unlike for the hemisphere, the dependence on the tip-surface convolution produces an inverse relationship in Young's modulus at larger surface-tip ratios. At the surface trough, the indenter has a maximum contact radius and the maximum surface interaction. Consequently, the indenter experiences a larger effective stiffness and Young's modulus. However, the contact radius decreases for scans away from wave trough, and Young's modulus decreases proportionally.

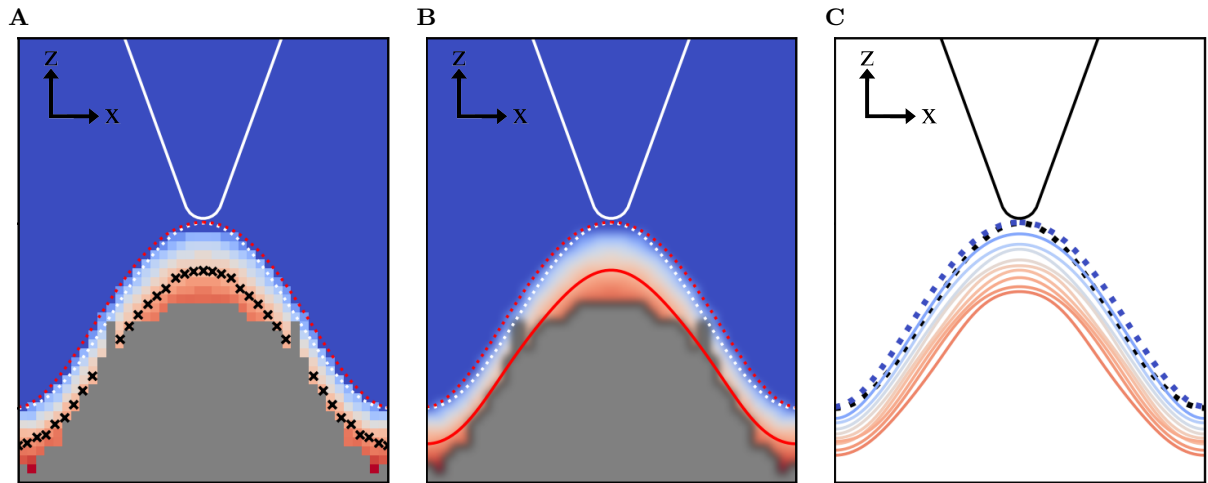


Figure 18: Illustrations of data produced from compression simulations for indenter $R/\lambda = 0.05$. (A) Raw two-dimensional heat map of indentation force over the scanning axis for the periodic structure. Including the point of constant force, $\frac{F}{E^*R^2} = 0.227$, shown as black crosses. These are points used to produce the force contours. The indenter is solid white, and the surface is dotted white. Points of zero force/ hard sphere contact is shown in dotted red.(B) Interpolated two-dimensional heat map of indentation force over the scanning axis for the periodic structure. Including overlayed contour of constant force, $\frac{F}{E^*R^2} = 0.227$, shown in solid red. The indenter is solid white, and the surface is dotted white. Points of zero force/ hard sphere contact is shown in dotted red. (C) Two-dimensional plot of force contours for varying indentation/ reference forces over the scanning axis of the periodic structure. Force shown varies within the limit of $0.227 < \frac{F}{E^*R^2} < 3.867$. The indenter and surface are black with initial zero force/ hard sphere boundary in dashed blue.

For greater quantitative analysis of the compression in the simulation, both Fourier analysis

and FWHM are employed. Fitting the contour points using a Fourier series allows us to break down the oscillatory signature of the simulated surface appearance. Furthermore, the individual contribution can highlight the deviation and behaviour of the surface when indented. The Fourier components are shown in Figure 20A . The zeroth component of the Fourier series represents a linear vertical offset. The increasing trend corresponds to an increased trough height for larger indenter-surface ratios. The first component corresponds to surface periodicity. Only this component is expected for the contour that matches the geometry of the surface, as shown by the black bar in Figure 20A . The decreasing amplitude of this component corresponds to an increase in surface distortion, as the amplitude is shared proportionally with higher-order terms. The second component is the significant component producing the widening wave peak, and higher-order terms refine the curvature of the contour.

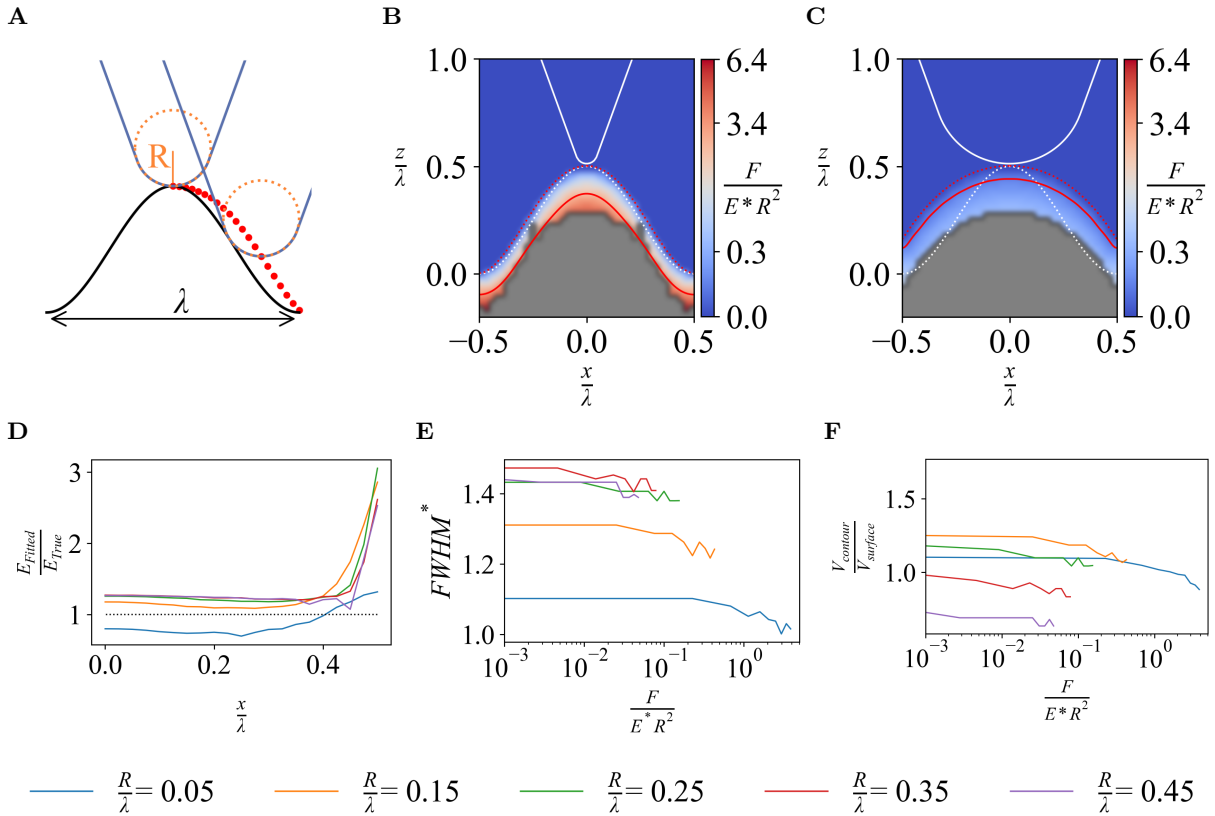


Figure 19: (A) Geometry of scan along the central axis of a hemisphere. Three-dimensional geometry is produced by rotating the indenter and extruding the wave. Wave is shown in black with wavelength λ . Indenter geometry is shown in blue with a circular tip of radius R in orange. Red points indicate initial scan positions (Hard sphere contact points). (B) Interpolated two-dimensional heat map of indentation force over the scanning axis for periodic structure with indenter $R/\lambda = 0.05$. Including overlayed contour of constant force, $\frac{F}{E^* R^2} = 0.227$, shown in solid red. The indenter is solid white, and the surface is dotted white. Points of zero force/ hard sphere contact is shown in dotted red. (C) Interpolated two-dimensional heat map of indentation force over the scanning axis for periodic structure with indenter $R/\lambda = 0.45$. Including overlayed contour of constant force, $\frac{F}{E^* R^2} = 0.227$, shown in solid red. The indenter is solid white, and the surface is dotted white. Points of zero force/ hard sphere contact is shown in dotted red. (D) Fitted Young's modulus over scan positions for each indenter radius (R/λ). (E) Relative FWHM of the contour divided by FWHM of true geometry ($FWHM^* = \frac{FWHM}{FWHM_{\text{True}}}$) variation over contour force for each indenter radius(R/λ). (F) Volume variation over contour force in spherical structures for each indenter(R/λ).

Therefore, the deviation from the true surface geometry and accuracy of the imaging can be quantified by analysing the variation of the first Fourier component over a range of contour forces. Analysing the absolute A1 for each contour force, shown in 20B , indicates how well we extract information from the surface topography. A lower indenter-surface ratio produces

less apparent structure deviation as the scan/tip more closely follows the surface geometry. Moreover, A1 is generally constant over the range of contour forces with only some decrease in the component for the smaller indenter at larger forces.

However, in contrast, the relative component A_1^* (i.e. individually normalised series where $A_1 + A_2 + A_3 + \dots = 1$) shows that although the absolute value of the first component may be constant throughout the forces range, the actual percentage of the series that the first component represents does vary. As shown in Figure 20C, when contour force increases, a greater percentage of the periodicity of the surface is recovered. This indicates that the apparent resolution extracted from the AFM image increases with indentation force. This could be due to the increased proportion of the indenter in contact with the surface and the elastic behaviour becoming more linear for deeper indentations. As a result, the indentations are subject to more influence from the surfaces. Therefore, variations in the surface geometry are better resolved in the contour at a higher force.

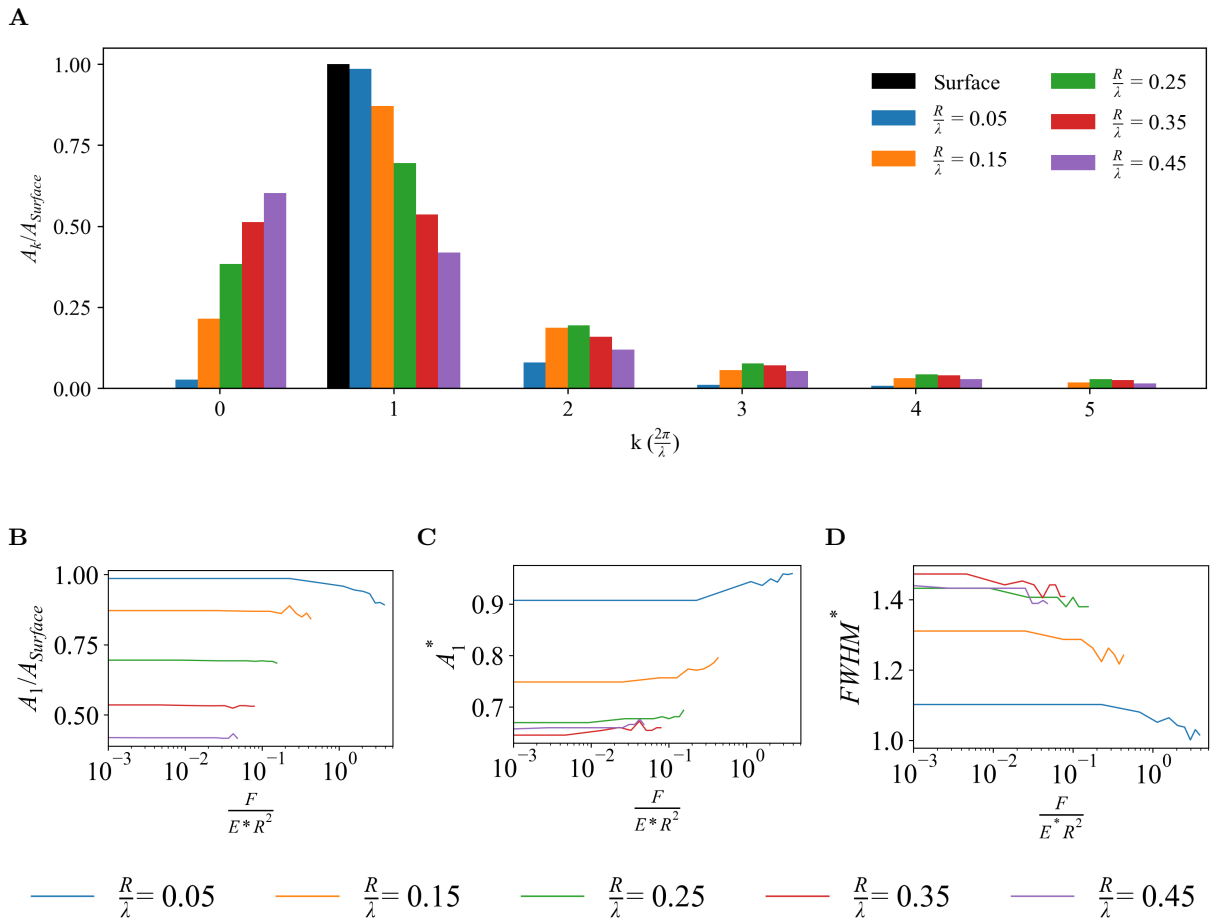


Figure 20: Analysis of force contours for periodic structure. (A) Fourier Series Component for force contours at $\frac{F}{E^*R^2} = 0.227$. (B) Variation of absolute component A_1 (Normalised by true surface amplitude/Fourier component) over contour force for a range of indenters ($\frac{R}{\lambda}$). (C) Variation of relative component A_1^* (A_1 coefficient normalised by series terms - $A_1^* = \sum_{k \neq 0} A_k$) over contour force for range of indenters ($\frac{R}{\lambda}$). (D) Relative FWHM of the contour divided by FWHM of true geometry ($FWHM^* = \frac{FWHM}{FWHM_{Surface}}$) variation over contour force for each indenter radius($\frac{R}{\lambda}$).

This behaviour is supported by the FWHM shown in Figure 17E. As the indentation force increases, FWHM decreases asymptotically, similarly to the absolute component A_1 , which represents the compression of the sample. This produces contours with FWHM closer to the true FWHM. Comparing this with the trends highlighted in Fourier analysis further reinforces that larger forces enable better resolution of the underlying structure. The initial constant trend of the FWHM may also show that at low forces, the compression around the midpoint of the

wave is low, and the indenter requires a large force to indent the slope region.

As shown in Figure 17F, the volume variation over indentation force is less prominent than for the hemisphere. For each indenter, there is only a slight reduction in volume as the indentation force increases. Moreover, unlike the hemisphere, the apparent volume is not directly proportional to the indenter's radius. Although a larger indenter produces greater tip convolution, which widens the peak, as volume is measured from the peak to the trough, the composite reduction in wave amplitude and depth results in a smaller volume overall as the indenter radius increases from $R/\lambda = 0.15$. In contrast, $R/\lambda = 0.15$ produces force contours closer to the topology of the surfaces, which is reflected in the apparent volume.

Overall, these analyses highlight similar characteristics to the hemisphere under compression. Young's modulus shows the dependence of elastic response/behaviour on the contact radius and tip convolution. Similarly, the volume highlights that the larger indenters/contact areas require larger forces to compress the sample to the same extent as smaller indenters. However, the FWHM and Fourier analysis elucidate a possible novel feature. The Fourier analysis demonstrates that larger indentation forces recover more surface periodicity.

3.3 FEM Applied to AFM Image Simulation of B-DNA

Finally, the FEM approach was applied to biomolecules to produce simulations of AFM imaging of DNA strands. As shown in Figure 21, we produced simulated images of a B-DNA DODE-CAMER/ DNA strand (PDB: 1bna). As detailed in the methodology, the biological surfaces were produced using a PDB file specifying the atoms' coordinates in the molecule. The simulation modelled 598 individual atoms using the van der Waals radius of the atoms. The biomolecule was produced in ABAQUS as an assembly of spheres for individual atoms. Atoms were merged to produce a composite sphere model of the biomolecule. The structure was modelled as a homogeneous elastic material with Young's modulus and Poisson ratio (1000 kPa and 0.3, respectively). The molecule was partially embedded in a rigid base/ substrate with the bottom 20% cleaved and fixed at the base using boundary conditions. The scan positions were then calculated in the base domain. The base itself was modelled as a rigid cube with width 52 Å and length 76 Å divided into bins of 4 Å producing 108 individual scan positions/ ABAQUS simulations. The AFM probe tip was modelled as a capped conical indenter, which was rigid and incompressible. The indenter had a radius of 4 Å and a conical half-angle 5°. The dynamics of an AFM raster scan were achieved by performing a set of individual indentation simulations across a surface domain. The AFM image was evaluated for a contour force of 0.1 pN. The code also allows hard-sphere model images to be calculated and produced along with the FEM shown in Figure 22B .

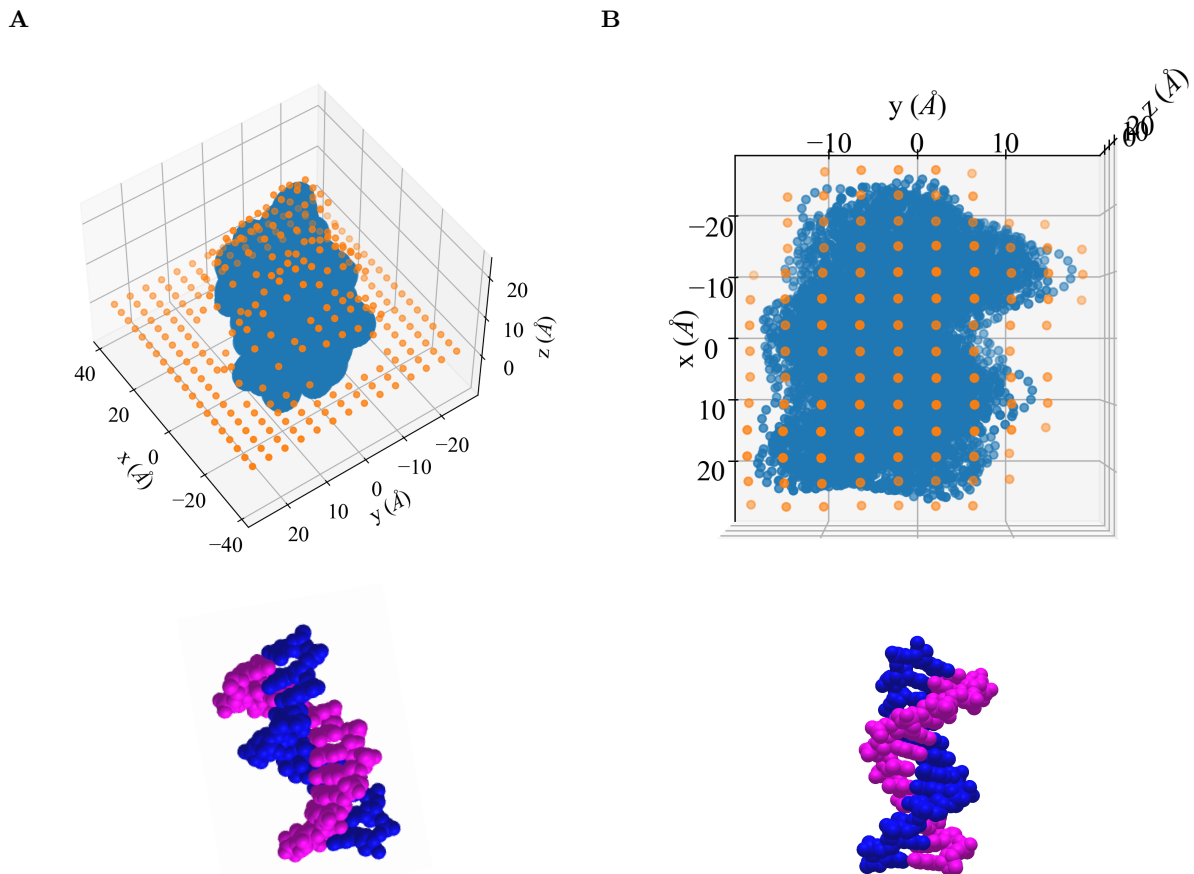


Figure 21: Illustration of biomolecule (blue) and scan positions for simulation (orange). Sphere model of PDB below each to aid in visualisation. (A) Side view of the assembly with all scan positions. (B) Top view of the assembly with clipped scan points (only points where tip interacts)

As presented in Figure 22A , our simulation has reproduced the expected appearance of the DNA double helix. This provides an example of the viability of the FEM approach to AFM imaging. We see distinct differences in the simulations produced with ABAQUS compared to the hard-

sphere model in Figure 22B . The indentation produces with FEM shows greater sensitivity for protruding features, whereas the deeper structure requires greater indentation/force to recover the surface topology. Similarly, simulating another orientation of the B-DNA, shown in Figure 22C , revealed the utility of the FEM approach. The base for these simulations was divided into bins of 10 Å producing 38 individual scan positions/ ABAQUS simulations. The AFM probe tip was modelled with a radius of 10 Å and a conical half-angle 10°. The FEM simulation reproduced more underlying helix structure than the hard-sphere model. The hard sphere model for this simulation gave a blurred image of the DNA as the large tip distorts the surface. The surface indentation produced by FEM appears to recover elements of the underlying structure. However, some of these variations originate from ABAQUS not performing calculations at the points of complex deformation. Within the code, these points are set to the maximum indentation depth so appear artificially deeper. This could pose challenges in repeatability.

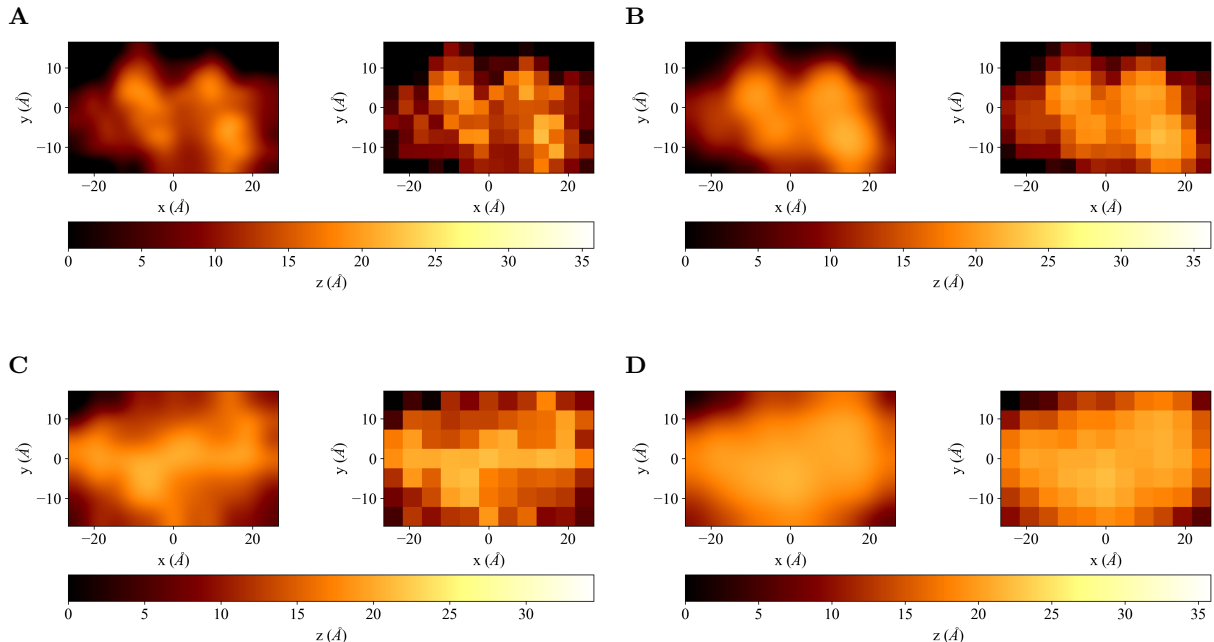


Figure 22: AFM images of a B-DNA DODECAMER with interpolated (left) and raw image(right) for each. (A) FEM Simulation with a tip radius of 4Å and spatial resolution of 4Å per pixel. (B) Hard sphere simulation with a tip radius of 4Å and spatial resolution of 4Å per pixel. (C) FEM simulation with a tip radius of 1nm and spatial resolution of 1nm per pixel.(D) Hard sphere simulation with a tip radius of 1nm and spatial resolution of 1nm per pixel.

4 Conclusion and Discussion

4.1 Conclusion

In conclusion, our FEM approach has demonstrated some novel and varied applications for the analysis of AFM imaging. Our analysis of the contact models for elastic half-spaces and spheres agreed with the theoretical models. Most prominently, the results highlight the under-fitting of the elastic modulus produced by simple Hertzian models for spherical samples. Moreover, our novel formulation of the Double Contact model for conical indenters demonstrated good predictive power over a range of surface radii.

Moreover, applying FEM to analyse the compression of hemispheres and simple periodic surfaces highlighted the quantitative power of this approach. These simulations highlighted the dependency of the elastic behaviour on the contact radius and tip convolution. Our results indicated that larger indenters require larger forces to compress the sample to the same extent. In addition, Fourier analysis of the simulated AFM contours elucidated a possible novel trend that larger indentation forces recover more of a surface's periodicity.

Finally, applying FEM to simulate the AFM appearance of B-DNA Dodecamer provides promising results. The code provides a range of parameters to allow simulations to emulate real AFM system specifications. These initial simulations showed the viability of this modelling and provided various extensions to be explored. However, this has shown some limitations to this approach, including the simulation times and scalability. For example, these simulations took around 48-72 hours for around 40 scan positions and one week for the 108 scan positions. These time scales limit the effectiveness of this approach for larger biomolecules. In addition, due to the numerical methods used by ABAQUS, deformation is limited and complex geometry simulations can often fail. This affects the repeatability and reliability of the simulation.

4.2 Discussion

These simulations have provided a good proof of concept, but large biomolecules would allow for better experimental comparison. Of interest would be the analysis of DNA compression during imaging and comparing it to experimental data. Furthermore, the analysis of human PARP-1 could add to current experimental efforts in the Hoogenboom lab. However, these require us to tackle the limitations discussed with scalability and time. Figure 23 shows the simulated hard sphere model for these two molecules to illustrate the scale. Greater computational resources may help mitigate the simulation time, and perhaps a courser grain may be required. This could help improve the repeatability issue produced by failed ABAQUS simulations caused by complex geometry.

Furthermore, an immediate improvement could involve simulations that account for biomolecule density, viscoelastic properties, and gravity. This could include modelling large biomolecules with multiple materials and properties and including adhesion in the model. In addition, introducing simulation of measurement and environmental errors, such as parachuting, noise, and thermal drift, could provide greater experimental applicability. Expanding the simulation to include in-situ conditions, such as liquid simulation, would provide an interesting extension in future work. This could be achieved using Abaqus/CFD, a Computational Fluid Dynamics software application which provides advanced computational fluid dynamics capabilities. In addition, Coulomb attraction of molecules can be included in ABAQUS.

Another extension could involve dynamic scans accounting for feedback and indentations based on threshold force. Using Abaqus/Explicit, more complex contact under transient loads can be modelled to include continuous raster scan such that change to a molecule in one indentation is carried over.

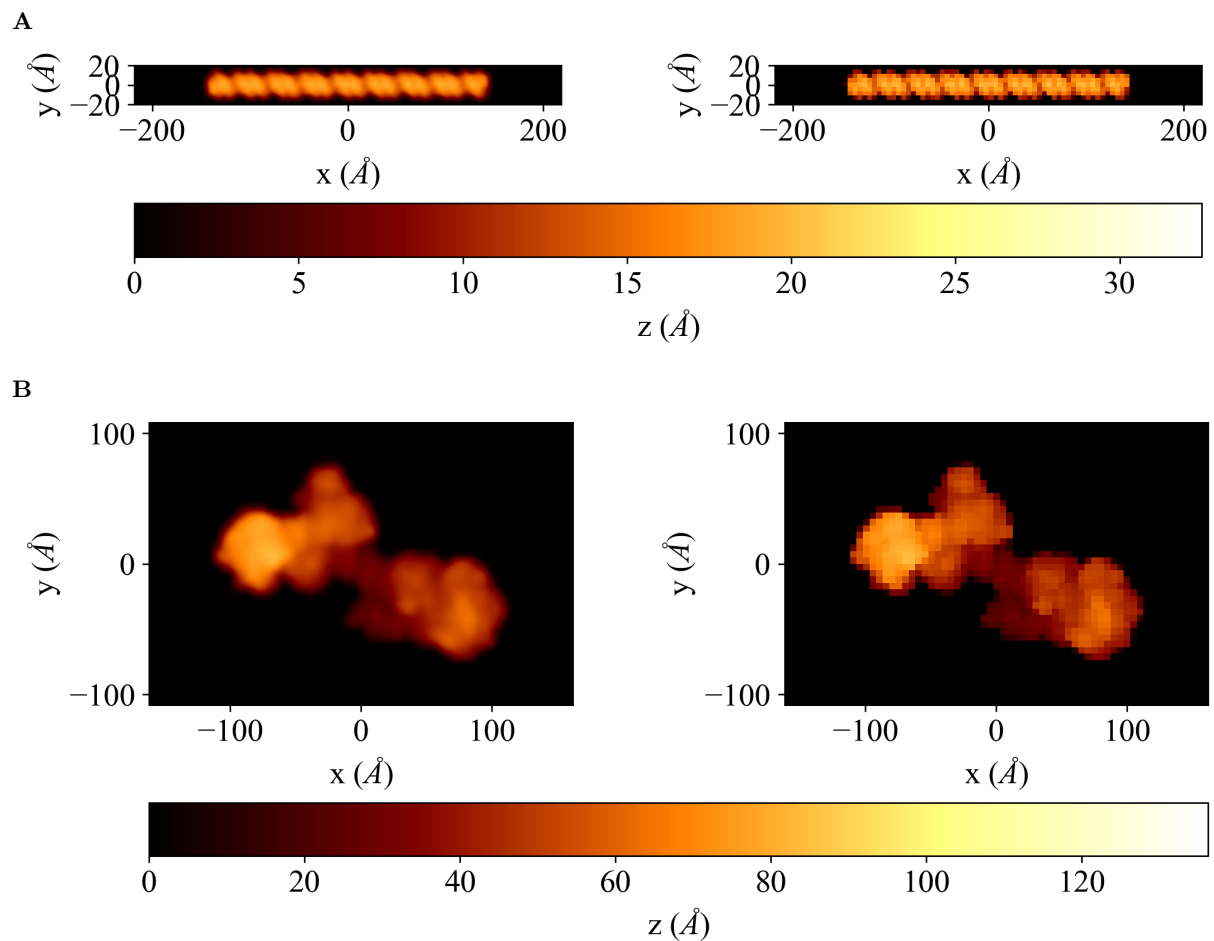


Figure 23: Hard sphere model simulations of AFM image (A) DNA strand (custom pdb). (B) Human PARP-1 (PDB:4dqy).

References

1. Nagashima, N., Matsuoka, S. & Miyahara, K. Nanoscopic hardness measurement by atomic force microscope. *JSME international journal. Ser. A, Mechanics and material engineering* **39**, 456–462 (1996).
2. Kempf, M., Göken, M. & Vehoff, H. Nanohardness measurements for studying local mechanical properties of metals. *Applied Physics A: Materials Science & Processing* **66** (1998).
3. Göken, M. & Kempf, M. Microstructural properties of superalloys investigated by nanoindentations in an atomic force microscope. *Acta Materialia* **47**, 1043–1052 (1999).
4. Yamamoto, A., Watanabe, A., Tsubakino, H. & Fukumoto, S. AFM observations of microstructures of deposited magnesium on magnesium alloys. *Materials science forum* **350**, 241–246 (2000).
5. Jalili, N. & Laxminarayana, K. A review of atomic force microscopy imaging systems: application to molecular metrology and biological sciences. *Mechatronics* **14**, 907–945 (2004).
6. Santos, N. C. & Castanho, M. A. An overview of the biophysical applications of atomic force microscopy. *Biophysical Chemistry* **107**, 133–149 (2004).
7. Amyot, R. & Flechsig, H. BioAFMviewer: An interactive interface for simulated AFM scanning of biomolecular structures and dynamics. *PLoS computational biology* **16**, e1008444 (2020).
8. Salapaka, S. M. & Salapaka, M. V. Scanning probe microscopy. *IEEE Control Systems Magazine* **28**, 65–83 (2008).
9. Binnig, G., Quate, C. F. & Gerber, C. Atomic Force Microscope. *Phys. Rev. Lett.* **56**, 930–933 (1986).
10. Eaton, P. & West, P. *Atomic force microscopy* (Oxford university press, 2010).
11. Yu, Y. *et al.* Atomic resolution imaging of halide perovskites. *Nano letters* **16**, 7530–7535 (2016).
12. Passeri, D. *et al.* Indentation modulus and hardness of polyaniline thin films by atomic force microscopy. *Synthetic metals* **161**, 7–12 (2011).
13. D'Antò, V. *et al.* Evaluation of surface roughness of orthodontic wires by means of atomic force microscopy. *The Angle Orthodontist* **82**, 922–928 (2012).
14. Dallaeva, D. *et al.* AFM imaging and fractal analysis of surface roughness of AlN epilayers on sapphire substrates. *Applied Surface Science* **312**, 81–86 (2014).
15. Acikgoz, O. & Baykara, M. Z. Speed dependence of friction on single-layer and bulk MoS₂ measured by atomic force microscopy. *Applied Physics Letters* **116**, 071603 (2020).
16. Zeng, X., Peng, Y. & Lang, H. A novel approach to decrease friction of graphene. *Carbon* **118**, 233–240 (2017).
17. Hughes, M. L. & Dougan, L. The physics of pulling polyproteins: a review of single molecule force spectroscopy using the AFM to study protein unfolding. *Reports on Progress in Physics* **79**, 076601 (2016).
18. Moody, J. & Allen, S. Atomic force microscopy: applications in biology. *Chemical Biology Applications and Techniques, Larijani B., Rosser, CA, Woscholski, R., Eds. John Wiley & Sons, Ltd., Hoboken, NJ, USA*, 29–45 (2006).
19. Wright, C. J. & Armstrong, I. The application of atomic force microscopy force measurements to the characterisation of microbial surfaces. *Surface and Interface Analysis* **38**, 1419–1428 (2006).
20. Dufrêne, Y. F. Using nanotechniques to explore microbial surfaces. *Nature Reviews Microbiology* **2**, 451–460 (2004).
21. Tyagi, A. K. & Malik, A. In situ SEM, TEM and AFM studies of the antimicrobial activity of lemon grass oil in liquid and vapour phase against *Candida albicans*. *Micron* **41**, 797–805 (2010).
22. Maghsoudy-Louyeh, S., Kropf, M. & Tittmann, B. Review of progress in atomic force microscopy. *The Open Neuroimaging Journal* **12** (2018).
23. Schitter, G., Steininger, J., Heuck, F. & Staufer, U. Towards fast AFM-based nanometrology and nanomanufacturing. *Int. J. of Nanomanufacturing* **8**, 392–418 (2012).

24. Dufrêne, Y. F. Atomic force microscopy, a powerful tool in microbiology. *Journal of bacteriology* **184**, 5205–5213 (2002).
25. Amyot, R., Marchesi, A., Franz, C. M., Casuso, I. & Flechsig, H. Simulation atomic force microscopy for atomic reconstruction of biomolecular structures from resolution-limited experimental images. *PLoS computational biology* **18**, e1009970 (2022).
26. Liu, Y., Mollaeian, K. & Ren, J. Finite element modeling of living cells for AFM indentation-based biomechanical characterization. *Micron* **116**, 108–115 (2019).
27. Han, R. & Chen, J. A modified Sneddon model for the contact between conical indenters and spherical samples. *Journal of Materials Research* **36**, 1762–1771 (2021).
28. Kontomaris, S. & Malamou, A. Hertz model or Oliver & Pharr analysis? Tutorial regarding AFM nanoindentation experiments on biological samples. *Materials Research Express* **7**, 033001 (2020).
29. Senda, Y., Blomqvist, J. & Nieminen, R. M. Computational model for noncontact atomic force microscopy: energy dissipation of cantilever. *Journal of Physics: Condensed Matter* **28**, 375001 (2016).
30. Roduit, C. *et al.* Stiffness tomography by atomic force microscopy. *Biophysical journal* **97**, 674–677 (2009).
31. Rajabifar, B., Wagner, R. & Raman, A. A fast first-principles approach to model atomic force microscopy on soft, adhesive, and viscoelastic surfaces. *Materials Research Express* **8**, 095304 (2021).
32. Zheng, Q., Zhu, H. & Yu, A. Finite element analysis of the contact forces between a viscoelastic sphere and rigid plane. *Powder Technology* **226**, 130–142 (2012).
33. Kontomaris, S.-V. The Hertz model in AFM nanoindentation experiments: applications in biological samples and biomaterials. *Micro and Nanosystems* **10**, 11–22 (2018).
34. Determination of Elastic Moduli of Thin Layers of Soft Material Using the Atomic Force Microscope. *Biophysical Journal* **82**, 2798–2810. ISSN: 0006-3495 (2002).
35. Dokukin, M. E., Guz, N. V. & Sokolov, I. Quantitative study of the elastic modulus of loosely attached cells in AFM indentation experiments. *Biophysical journal* **104**, 2123–2131 (2013).
36. Glaubitz, M. *et al.* A novel contact model for AFM indentation experiments on soft spherical cell-like particles. *Soft Matter* **10**, 6732–6741 (2014).
37. Kontomaris, S., Stylianou, A., Nikita, K. & Malamou, A. Determination of the linear elastic regime in AFM nanoindentation experiments on cells. *Materials Research Express* **6**, 115410 (2019).
38. Chen, Z., Luo, J., Doudevski, I., Erten, S. & Kim, S. H. Atomic Force Microscopy (AFM) Analysis of an Object Larger and Sharper than the AFM Tip. *Microscopy and Microanalysis* **25**, 1106–1111 (2019).
39. Kontomaris, S.-V. & Malamou, A. The harmonic motion of a rigid cylinder on an elastic half-space. *European Journal of Physics* **41**, 015003 (2019).
40. Vinckier, A. & Semenza, G. Measuring elasticity of biological materials by atomic force microscopy. *FEBS letters* **430**, 12–16 (1998).
41. Korayem, M. & Taheri, M. Modeling of various contact theories for the manipulation of different biological micro/nanoparticles based on AFM. *Journal of nanoparticle research* **16**, 1–18 (2014).
42. Harding, J. & Sneddon, I. *The elastic stresses produced by the indentation of the plane surface of a semi-infinite elastic solid by a rigid punch* in *Mathematical Proceedings of the Cambridge Philosophical Society* **41** (1945), 16–26.
43. Johnson, K. L., Kendall, K. & Roberts, a. Surface energy and the contact of elastic solids. *Proceedings of the royal society of London. A. mathematical and physical sciences* **324**, 301–313 (1971).
44. Derjaguin, B. V., Muller, V. M. & Toporov, Y. P. Effect of contact deformations on the adhesion of particles. *Journal of Colloid and interface science* **53**, 314–326 (1975).

45. Burnham, N. A. & Kulik, A. J. in *Handbook of Micro/Nano Tribology* 247–271 (CRC Press, 2020).
46. Carpick, R. W., Ogletree, D. F. & Salmeron, M. A general equation for fitting contact area and friction vs load measurements. *Journal of colloid and interface science* **211**, 395–400 (1999).
47. Pietrement, O. & Troyon, M. General equations describing elastic indentation depth and normal contact stiffness versus load. *Journal of colloid and interface science* **226**, 166–171 (2000).
48. Sun, Y., Akhremtchev, B. & Walker, G. C. Using the adhesive interaction between atomic force microscopy tips and polymer surfaces to measure the elastic modulus of compliant samples. *Langmuir* **20**, 5837–5845 (2004).

Appendix

A Notation

δ - Indentation depth of the indenter into surface

δ_{12} - Indentation displacement of the indenter

δ_{32}^* - Indentation depth of the surface into base

F Total force of indentation

F_{12} - Contact force experienced by indenter

F_{32} - Contact force experienced by base

R_{12} - Tip-surface contact radius

R_1/R - Indenter radius

R_2/r - Surface radius

$$\frac{1}{R_{12}} = \frac{1}{R_1} + \frac{1}{R_2},$$

h - Surface radius/depth

α - Indenter principle angle

E_2/E - Young's modulus

ν_2 - Poisson's ratio of the sample

B Models of Indentation in Atomic Force Microscopy

B.1 Hertz Model

The Hertz model is the most prevalent model used for AFM indentation and describes contact forces for isotropic and homogeneous materials, denoted as elastic half-spaces, which present a linearly elastic response to forces³⁷ and are assumed to extend infinitely in all directions with a flat boundary on the top surface.³⁹ This necessitates the AFM tip radius be at least ten times smaller than the sample dimension for the assumption to hold. In addition, it is assumed that the contract is smooth and continuous with no friction or adhesion³⁷.

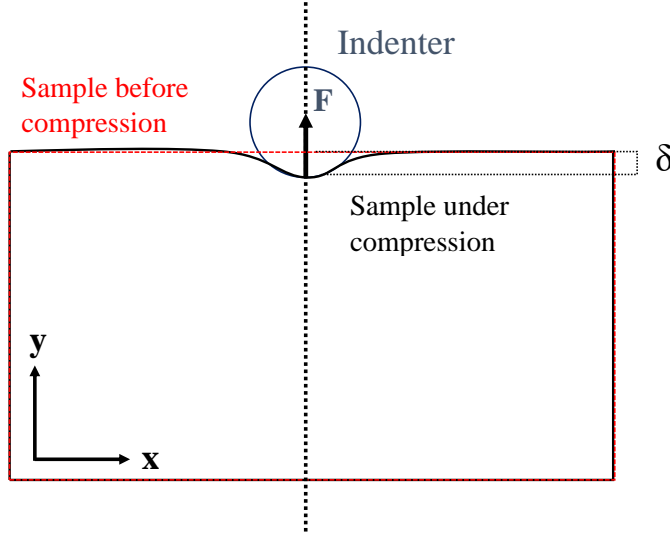


Figure 24: Illustration of contact experienced by elastic half-space. Where δ is indentation depth of the indenter into surface, F is total force of indentation.

Subsequently, the Hertz model provides the relation between the applied force, F , and the indentation depth, δ ^{28,33}

$$F_{Hertz}(\delta) = \frac{4}{3} \frac{E_2}{(1 - \nu_2^2)} \sqrt{R_{12}} \delta^{3/2} \quad (2)$$

$$\frac{1}{R_{12}} = \frac{1}{R_1} + \frac{1}{R_2}$$

where R_{12} is the tip-surface contact radius, R_1 is indenter radius, R_2 is surface radius (inf for a plane) E_2 Young's modulus and ν_2 is the Poisson's ratio of the sample. This relation allows calculation of Young's modulus as a fitting parameter for experimental measurements of force curves^{35,36,40}. In addition, taking the logarithm of this equation returns a linear equation:

$$\log(F_{Hertz}(\delta)) = \frac{3}{2} \log(\delta) + \log\left(\frac{4}{3} \frac{E_2}{(1 - \nu_2^2)} \sqrt{R_{12}}\right) \quad (3)$$

Subsequently, this equation can be used to cast indentation data in dimensional units of force ($\frac{F}{E^* R^2}$) and indentation (δ/R), such that:

$$\frac{F_{Hertz}(\delta)}{E^* R_{12}^2} = \frac{4}{3} \left(\frac{\delta}{R_{12}}\right)^{3/2} \quad (4)$$

$$F_{Dimensionless} = \frac{4}{3} (\delta_{Dimensionless})^{3/2} \quad (5)$$

where $E^* = \frac{E_2}{(1-\nu_2^2)}$. Therefore, $F_{Dimensionless} = \frac{F_{Hertz}}{E^* R_{12}^2}$ and $\delta_{Dimensionless} = \frac{\delta}{R_{12}}$.

B.2 Other Hertzian Model

The Hertz model ignores adhesive and frictional forces and can only be applied for parabolic tips (and approximately for a spherical tip given that $h \ll R$). However, various other 'Hertzian' contact models⁴¹, including the models of Sneddon^{27,42}, JKR⁴³, DMT⁴⁴, BCP⁴⁵, COS⁴⁶, PT⁴⁷, and SUN⁴⁸, use the same base dynamics but incorporate various other adhesive forces, tip geometry and dynamics, and constraints to obtain more advanced models of contact mechanics. Some other models used are discussed below.

B.3 Dimitriadiis Model

A more complex model that is applied to spherical indenters for soft materials in AFM experiment is the model by Dimitriadiis *et al*³⁴.

$$F_{Dimitriadiis}(\delta) = \frac{4}{3} \frac{E_2}{(1-\nu_2^2)} R_{12}^{1/2} \delta^{3/2} \left[1 - \frac{2\alpha_0}{\pi} \chi + \left(\frac{2\alpha_0}{\pi} \chi \right)^2 - \left(\frac{2\alpha_0}{\pi} \chi \right)^3 + \left(\frac{2\alpha_0}{\pi} \chi \right)^4 - \frac{16}{\pi^2} \beta_0 \left(\frac{2\pi}{15} - \frac{3}{5} \alpha_0 \chi \right) \chi^3 \right] \quad (6)$$

where R_{12} is the radius of contact between the tip and the surface $\frac{1}{R_{12}} = \frac{1}{R_1} + \frac{1}{R_2}$, R_1 is the indenter radius, R_2 is the surface radius (inf for a plane) Young's modulus E_2 and ν_2 is the Poisson's ratio of the sample. And

$$\begin{aligned} \chi &= \frac{\sqrt{R_{12}\delta}}{h} \\ \alpha_0 &= -0.347 \frac{3-2\nu_2}{1-\nu_2} \\ \beta_0 &= 0.056 \frac{5-2\nu_2}{1-\nu_2} \end{aligned}$$

B.4 Sneddon Model

Applying the Hertz model to conical indenters, we recover the Sneddon model²⁷ given as

$$F_{Sneddon}(\delta) = \frac{2}{\pi} \frac{E_2}{(1-\nu_2^2)} \tan(\alpha) \delta^2 \quad (7)$$

where α is indenter principle angle, R_2 is surface radius (inf for a plane) E_2 Young's modulus and ν_2 is the Poisson's ratio of the sample. In addition, taking the logarithm of this equation returns a linear equation:

$$\log(F_{Sneddon}(\delta)) = 2 \log(\delta) + \log \left(\frac{2}{\pi} \frac{E_2}{(1-\nu_2^2)} \tan(\alpha) \right) \quad (8)$$

B.5 Double Contact Model

Indentation into elastic spheres presents a more complex analysis as we must account for both the indentation between the indenter and the surface and the indentation between the surface and the base. As seen in Figure 25, part of the indenter of the displacement is due to the compression of the elastic sphere into the base δ_{32}^* . Moreover, the reaction force between the indenter and sphere will be enhanced as the indenter creates reaction force both due to its indentation into the sample and due to the compression of the sample between the indenter and base. To account for this, we consider double contact models^{35,36}.

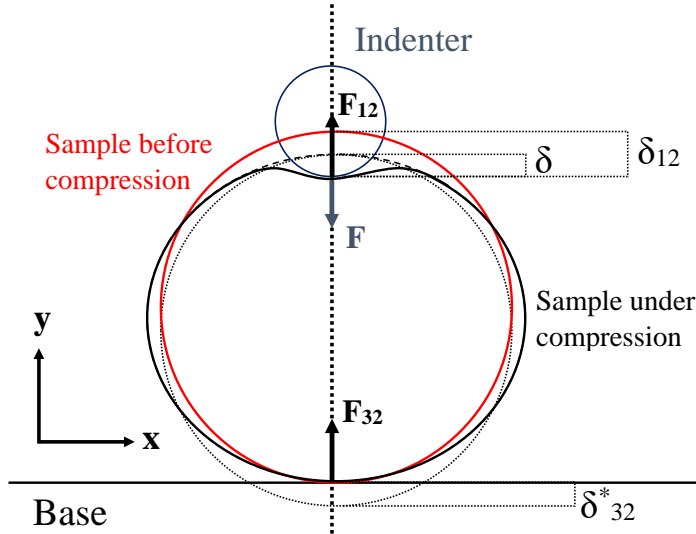


Figure 25: Illustration of double contact experienced by spherical sample. Where δ is indentation depth of the indenter into surface, δ_{12} is total displacement of the indenter, δ_{32}^* indentation depth of the surface into base, F is total force of indentation, F_{12} is contact force experienced by indenter, F_{32} contact force experienced by base. In these models, the corrected values for indentation depth are calculated by subtracting the displacement/ compression of the surface at its base from the displacement of the indenter. For the corrected force, we sum the reaction force between the indenter and surface and the force between the base and surface. This is as the force due to the indenter will be distributed between both the reaction at the base and the indenter.

In these models, the corrected values for indentation depth are calculated by subtracting the displacement/ compression of the surface at its base from the displacement of the indenter.

$$\delta = \delta_{12} - \delta_{32}^* \quad (9)$$

where δ indentation depth of the indenter into surface, δ_{12} is indentation displacement of the indenter, δ_{32}^* indentation depth of the surface into base. For the corrected force, we sum the reaction force between the indenter and surface and the force between the base and surface. This is as the force due to the indenter will be distributed between both the reaction at the base and the indenter.

$$F = F_{12} + F_{32} \quad (10)$$

where F is total force of indentation, F_{12} is contact force experienced by indenter, F_{32} contact force experienced by base.

B.6 Hertz Double Contact

Surface - Spherical Indenter Indentation (Hertz)

$$\delta_{12}(F) = \left(\frac{3}{4} \frac{(1 - \nu_2^2)}{E_2} \frac{F}{\sqrt{R_{12}}} \right)^{2/3} \quad (11)$$

Spherical Surface

$$\frac{1}{R_{12}} = \frac{1}{R_1} + \frac{1}{R_2}$$

Flat Surface

$$R_{32} = R_2$$

Calculating Double Contact

$$\begin{aligned} \delta_{12}(F) &= \delta(F) + \delta_{32}^*(F) \\ &= \left(\frac{3}{4} \frac{(1 - \nu_2^2)}{E_2} \frac{F}{\sqrt{R_{12}}} \right)^{2/3} + \left(\frac{3}{4} \frac{(1 - \nu_2^2)}{E_2} \frac{F}{\sqrt{R_{32}}} \right)^{2/3} \\ &= \left(\frac{3}{4} \frac{(1 - \nu_2^2)}{E_2} \cdot F \right)^{2/3} \left[\frac{1}{R_{12}^{1/3}} + \frac{1}{R_{32}^{1/3}} \right] \\ &= \left(\frac{3}{4} \frac{(1 - \nu_2^2)}{E_2} \cdot F \right)^{2/3} \left[\frac{R_{12}^{1/3} + R_{32}^{1/3}}{(R_{12}R_{32})^{1/3}} \right] \\ F(\delta_{12}) &= \frac{4}{3} \frac{E_2}{(1 - \nu_2^2)} \left[\frac{(R_{12}R_{32})^{1/3}}{R_{12}^{1/3} + R_{32}^{1/3}} \right]^{3/2} \delta_{12}^{3/2} \end{aligned} \quad (12)$$

where δ indentation depth of the indenter into surface, δ_{12} is indentation displacement of the indenter, δ_{32}^* indentation depth of the surface into base and F is contact force experienced by indenter. R_{12} is the tip-surface contact radius, R_{32} is the surface-base contact radius, R_1 is indenter radius, and R_2 is surface radius. E_2 Young's modulus and ν_2 is the Poisson's ratio of the sample.

B.7 Hertz-Sneddon Double Contact

Using a similar methodology for Sneddon and Hertz we formulate our own double contact model for conical indenters:

Model for Surface - indenter (Sneddon)

$$\delta_{12}(F) = \left(\frac{\pi}{2} \frac{(1 - \nu_2^2)}{E_2} \frac{F}{\tan(\alpha)} \right)^{1/2}$$

Model for Surface-Base Indentation (Hertz)

$$\delta_{32}(F) = \left(\frac{3}{4} \frac{(1 - \nu_2^2)}{E_2} \frac{F}{\sqrt{R_{32}}} \right)^{2/3}$$

Flat Surface

$$R_{32} = R_2$$

Calculating Double Contact

$$\delta(F) = \delta_{12}(F) + \delta_{32}^*(F)$$

$$= \left(\frac{\pi}{2} \frac{(1 - \nu_2^2)}{E_2} \frac{F}{\tan(\alpha)} \right)^{1/2} + \left(\frac{3}{4} \frac{(1 - \nu_2^2)}{E_2} \frac{F}{\sqrt{R_{32}}} \right)^{2/3}$$

Let the conical term dominate, and for the spherical term $2/3 \approx 1/2$

$$= \left(\frac{3}{4} \frac{(1 - \nu_2^2)}{E_2} F \right)^{1/2} \left(\frac{1}{R_{32}}^{1/4} + \left(\frac{2\pi}{3} \frac{1}{\tan(\alpha)} \right)^{1/2} \right) \quad (13)$$

$$F(\delta_{12}) = \frac{4}{3} \frac{E_2}{(1 - \nu_2^2)} \left[\frac{1}{\left(\frac{1}{R_{32}}^{1/4} + \left(\frac{2\pi}{3} \frac{1}{\tan(\alpha)} \right)^{1/2} \right)} \right]^2 \delta_{12}^2 \quad (14)$$

where δ indentation depth of the indenter into surface, δ_{12} is indentation displacement of the indenter, δ_{32}^* indentation depth of the surface into base and F is contact force experienced by indenter. R_{12} is the tip-surface contact radius, R_{32} is the surface-base contact radius, R_1 is indenter radius, and R_2 is surface radius. E_2 Young's modulus and ν_2 is the Poisson's ratio of the sample.

C Tip Convolution for Hard Sphere Model

From geometry:

$$\cos(\alpha) = \frac{X_{tip}}{R_{surface} + R_{tip}} \quad (15)$$

$$\sin(\alpha) = \frac{Z_{tip} + R_{tip}}{R_{surface} + R_{tip}} \quad (16)$$

From trigonomerty:

$$\sin(\alpha) = \frac{\sqrt{(R_{surface} + R_{tip})^2 - X_{tip}^2}}{R_{surface} + R_{tip}} \quad (17)$$

Therefore:

$$\frac{\sqrt{(R_{surface} + R_{tip})^2 - X_{tip}^2}}{R_{surface} + R_{tip}} = \frac{Z_{tip} + R_{tip}}{R_{surface} + R_{tip}} \quad (18)$$

$$Z_{tip} = \sqrt{(R_{surface} + R_{tip})^2 - X_{tip}^2} - R_{tip} \quad (19)$$

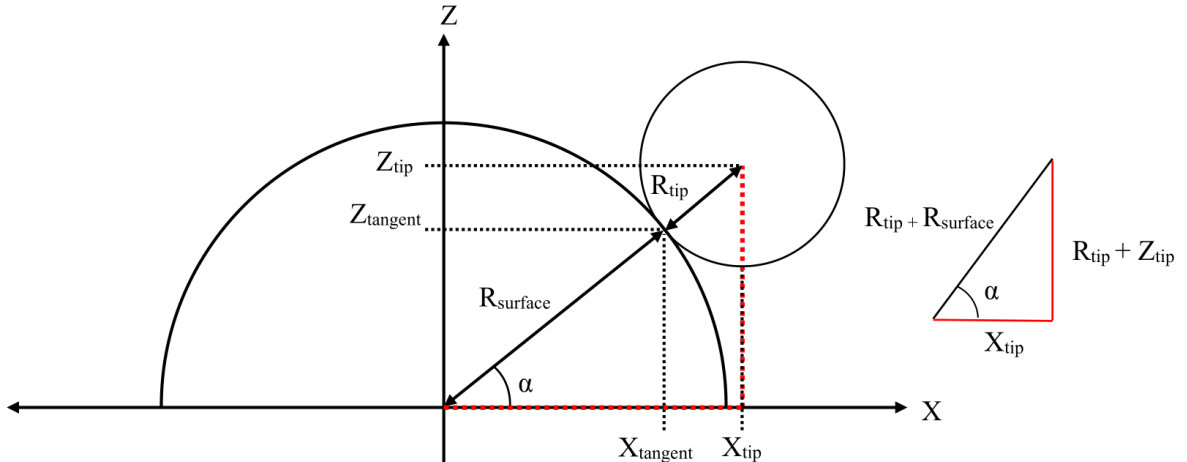


Figure 26: Example two dimensional heat map of indentation force over the scanning axis for semi-sphere structure. Including overlayed contour of constant force